Journal of Environmental Chemical Engineering 13 (2025) 119735

Contents lists available at ScienceDirect

Journal of Environmental Chemical Engineering

journal homepage: www.elsevier.com/locate/jece

Synergistic PMS activation by N-bridged spider-web-like nanocopper wires on kapok-derived carbon for efficient removal of organic pollutants

Shenghui Wang [a], Yanhua Song [a,*], Bin Wang [b,c], Xingwang Zhu [d], Xue Gao [b], Zhiyi Xu [b], Fujing Zhang [a], Jinyuan Liu [b,c,**], Paul K. Chu [c,*]

[a] School of Environmental and Chemical Engineering, Jiangsu University of Science and Technology, Zhenjiang, Jiangsu 212003, China
[b] Institute for Energy Research, School of the Environment and Safety Engineering, Jiangsu University, Zhenjiang, Jiangsu 212013, China
[c] Department of Physics, Department of Materials Science and Engineering, and Department of Biomedical Engineering, City University of Hong Kong, Tat Chee Avenue, Kowloon 999077, Hong Kong, China
[d] Institute of Technology for Carbon Neutralization, College of Environmental Science and Engineering, Yangzhou University, Yangzhou 225009, China

ARTICLE INFO

Keywords:
Biomass-derived carbon
Spider-web-like structures
Reactive oxygen species
Environmental remediation
Cu-based catalysts

ABSTRACT

Transition metallic copper has garnered significant attention in advanced oxidation processes (AOPs) due to its exceptional ability to activate peroxymonosulfate (PMS) *via* redox cycling and electron transfer. Herein, spider-web-like Cu nanowires are stabilized on kapok-derived carbon-tubes by nitrogen-bridging, reduce charge transfer resistance. Unlike conventional nanoparticles, metallic Cu nanowires exist in the highly dispersed nanoweb structure along the carbon-tube surface. The Cu-N-C structure serves as the primary active site for PMS activation and boasts a tetracycline hydrochloride (TCH) degradation rate that is 3.17 times higher than that of the KTC/PMS system, and it exhibits a stronger catalytic effect under alkaline conditions. Reactive oxygen species (ROS), particularly $\bullet O_2^-$ and $^1O_2$, are the key contributors in the radical and non-radical degradation pathways, respectively. Our results reveal that the incorporation of nitrogen reduces the electron transfer resistance, while the Cu-N site formed by Cu and pyrrole nitrogen facilitates electron transfer and the activation of PMS. The activity recovery rate after the material undergoes recycling can reach 100 %. The toxicity experiments conducted on E. coli showed that the degradation products, the dosage of PMS, and the material itself have extremely low toxicity to E. coli. These results highlight the synergistic effect of N-bridging and spider-web Cu morphology in achieving efficient, sustainable, and practical PMS activation for environmental remediation.

1. Introduction

Conventional wastewater treatment processes are often ineffective for removing persistent pollutants, such as pharmaceuticals, pesticides, industrial chemicals, and dyes [1,2]. Tetracycline hydrochloride (TCH) possesses a complex molecular structure with multiple functional groups, rendering it highly resistant to photolysis, biodegradation, and conventional chemical oxidation. Consequently, it tends to persist in aquatic environments, posing potential risks to ecosystems and public health [3]. In this context, advanced oxidation processes (AOPs) have attracted increasing attention due to their ability to mineralize organic contaminants via the generation of highly reactive oxidizing species, including hydroxyl radicals (•OH) and sulfate radicals ($SO_4\bullet^-$) [4] [5]. Among various AOPs, peroxymonosulfate (PMS)-based systems are particularly promising because of their strong oxidation potential, capability to produce multiple reactive oxygen species, and relatively low operational costs [6,7]. PMS can be activated through several pathways, such as ultraviolet light irradiation, thermal treatment, and catalysis using metals, carbon-based materials, or their composites [8–11]. An ideal catalyst should efficiently activate PMS while maintaining high stability and recyclability. However, most conventional catalysts suffer from low reactivity and poor durability of active sites, which significantly limits their performance in PMS activation. Therefore, the development of advanced catalytic materials with enhanced activity and long-term stability is urgently needed [12].

Carbonaceous materials have unique physicochemical characteristic

* Corresponding authors.
** Corresponding author at: Institute for Energy Research, School of the Environment and Safety Engineering, Jiangsu University, Zhenjiang, Jiangsu 212013, China.
E-mail addresses: songyh@just.edu.cn (Y. Song), jyliu@ujs.edu.cn (J. Liu), paul.chu@cityu.edu.hk (P.K. Chu).

https://doi.org/10.1016/j.jece.2025.119735
Received 14 July 2025; Received in revised form 13 September 2025; Accepted 9 October 2025
Available online 10 October 2025

[13], such as excellent thermal stability, abundant surface functional groups, superior electrical conductivity, and large specific surface area [14–16], rendering them suitable for AOPs [17]. For instance, biomass-derived carbonaceous materials, which have green, sustainable, and economical merits [18,19], can be produced from biological waste using simple and environmentally friendly carbonization and chemical modification methods [20,21]. However, challenges such as the limited number of active sites, insufficient electron transfer capability, and deactivation during catalytic reactions have hampered wider applications of biomass-derived carbon [22,23]. Researchers have attempted to optimize the surface properties of biomass-derived carbon by doping with nitrogen [24,25], sulfur [26], phosphorus [27], and metals to enhance the catalytic activity [28]. In particular, nitrogen doping enhances the number of active sites, modifies the electronic structure of the materials, and improves the efficiency of PMS activation. Wang et al. prepared nitrogen-doped biochar using corncob and urea to activate peroxydisulfate (PDS) for pollutant degradation, with experimental evidence highlighting the critical contribution of edge-nitrogen configurations in enhancing electron transport pathways [29]. Additionally, the incorporation of transition metals such as Fe [30], Co [31], Cu [32,33], Bi [34,35], and Ni [36] has been shown to activate PMS by electron donation and accelerate the reactions. In particular, Cu plays dual roles of coordinating with PMS to generate ROS and enhancing electron transfer. Chen et al. have developed single-atom Cu-loaded carbon to activate PMS and various antibiotics [37]. However, the high metal leaching rate and limited recyclability hinder large-scale applications. To overcome the aforementioned drawbacks, combining nitrogen and metal doping is a promising strategy. Cu can coordinate with nitrogen to form electron-deficient carbon structures, while nitrogen stabilizes Cu in the materials and reduces metal leaching. For instance, Wu et al. have used sodium alginate to prepare Cu-N-doped biochar that can degrade drugs within 15 min in spite of relatively low pollutant concentrations [38]. Nitrogen creates electron-rich regions and provides electrons to the metal *via* coordinating bonds, while the metal accepts electrons through its vacant orbitals to facilitate electron transfer and promote PMS activation by generating highly reactive species. The synergistic effects enhance the catalytic efficiency and stability [39].

Herein, a nitrogen-bridged spider-web-like copper nanowire catalyst anchored on kapok-derived carbon (0.6-Cu-N-KTC) was designed to overcome the limitations of conventional Cu-based PMS activators. This architecture, constructed via Cu-N-C coordination, enables uniform copper dispersion, inhibits agglomeration, and establishes an interconnected conductive network that facilitates rapid electron transfer [40]. Such a structural configuration exposes abundant active sites and enhances both radical ($\bullet O_2^-$, $SO_4^{\bullet-}$) and dominant non-radical ($^1O_2$) PMS activation pathways. Catalytic performance for tetracycline hydrochloride (TCH) degradation across a wide pH range (1−13) was systematically evaluated, reactive oxygen species contributions were quantified using scavenger tests and ESR, and long-term stability, recyclability, and environmental safety were assessed. These findings reveal the pivotal role of N-bridging in optimizing Cu-based PMS systems and present a scalable strategy for sustainable water purification.

2. Material and methods

2.1. Chemicals and reagents

The Kapok fibers were purchased from Indonesia and PMS was obtained from Shanghai Aladdin Biochemical Technology Co., Ltd. Copper chloride dihydrate ($CuCl_2{\cdot}2\ H_2O$), melamine, potassium ferricyanide, potassium ferrocyanide, tert-butanol (TBA), potassium thiocyanate (KSCN), dimethyl sulfoxide (DMSO), disodium ethylenediaminetetraacetate (EDTA-2Na), L-tryptophan (L-Trp), p-benzoquinone (p-BQ), tripotassium phosphate, potassium nitrate, potassium chloride, sodium chloride, potassium bicarbonate, and humic acid (HA) were purchased from Shanghai Macklin Biochemical Technology Co., Ltd. Anhydrous ethanol and methanol were obtained from Chinasun Specialty Products Co., Ltd., and LB agar was purchased from Guangdong Huankai Microbial Technology Co., Ltd. Furfuryl alcohol (FFA), atrazine (ATZ), sulfamethoxazole (SMX), ciprofloxacin (CIP), p-chlorophenol (4-CP), bisphenol A (BPA), 2,4-dichlorophenol (2,4-DCP), phenol, and ranitidine (RAN) were bought from China National Medicines Corporation Ltd. All the chemicals were used without purification, and deionized water (resistivity of 18.25 MΩ cm^{-1}) was used in the experiments.

2.2. Preparation of materials

The kapok fibers were rinsed with DI water three times to remove dried and impurities at 60°C for 16 h. The dried kapok fibers (0.5 g) were calcined in a tube furnace at a heating rate of 5 °C/min under nitrogen at 800 °C for 2 h to obtain kapok tidbits biomass-carbon (KTC).

The 0.6-Cu-N-KTC synthesis is shown in Fig. 1**a**. Melamine (1 g) was dissolved in 50 mL of anhydrous ethanol and sonicated to attain full dispersion. $CuCl_2{\cdot}2\ H_2O$ powder was added and sonicated for 20 min, followed by the introduction of 0.5 g of the kapok fibers to the mixture and further sonication for 20 min. It was heated in a beaker with boiling water bath (100 °C) until complete evaporation of the ethanol solvent. Carbonization of the green kapok fibers was carried out in a covered alumina crucible, samples were heated to 800 °C for 2 h at rate of 5 °C/min under continuous N_2 flow, ultimately producing a black product. The black product was stirred in 100 mL of 2 mol/L H_2SO_4 for 24 h to remove Cu from the surface. A sand core filter was used to rinse the solution with deionized water until the pH = 7. The product was then dried at 60 °C for 12 h. This product was named x-Cu-N-KTC, where x was the amount of $CuCl_2{\cdot}2\ H_2O$ used, that is, 0.2 g, 0.4 g, 0.6 g, 0.8 g, and 1.0 g (0.2-Cu-N-KTC, 0.4-Cu-N-KTC, 0.6-Cu-N-KTC, 0.8-Cu-N-KTC, and 1.0-Cu-N-KTC), while the control without the addition of $CuCl_2{\cdot}2\ H_2O$ was designated as N-KTC. After 0.6-Cu-N-KTC was determined to have the optimal properties, melamine was omitted from the synthesis to obtain 0.6-Cu-KTC.

2.3. Catalytic degradation

The pollutant degradation studies were performed under ambient temperature conditions. The catalyst was added to a 50 mL beaker containing 25 mL of 30 mg/L TCH and stirred in the dark for 20 min to achieve adsorption-desorption equilibrium. A sample was taken and then after the addition of PMS, 2 mL sample was taken. The samples were filtered through a 0.22 μm mixed cellulose ester (MCE) membrane and mixed vigorously with 1 mL of methanol. Quantitative analysis of TCH concentration and its decomposition efficiency was achieved through UV-Vis spectroscopic monitoring at the characteristic absorption wavelength of 356 nm.

2.4. Toxicity evaluation

To assess the biotoxicity of the materials, the Escherichia coli activity was monitored. The water, saline solution, culture medium, and instruments were sterilized at 121 °C for 15 min. A 30 mg/L TCH solution was prepared using sterilized water and placed on Petri dishes. The bacterial suspension was diluted to approximately 10^7 cfu/mL, and 1 mL of the suspension was added to each sterilized centrifuge tube. Afterward, 9 % NaCl (201 μL) was added to 2 mL of the degradation solution, which was placed in a centrifuge tube containing the bacterial suspension and shaken for 15 s. Subsequently, the solution (150 μL) was spread on the surface of the culturing medium and incubated at 37°C for 18 h. The Escherichia coli cells were mixed with the degradation solution, washed twice with saline, and fixed for 2 h in 3:1 methanol:acetic acid. The sample was treated with 50 %, 70 %, 85 %, 90 %, and 100 % ethanol sequentially for 10 min, coated with gold, and examined by scanning electron microscopy (SEM).

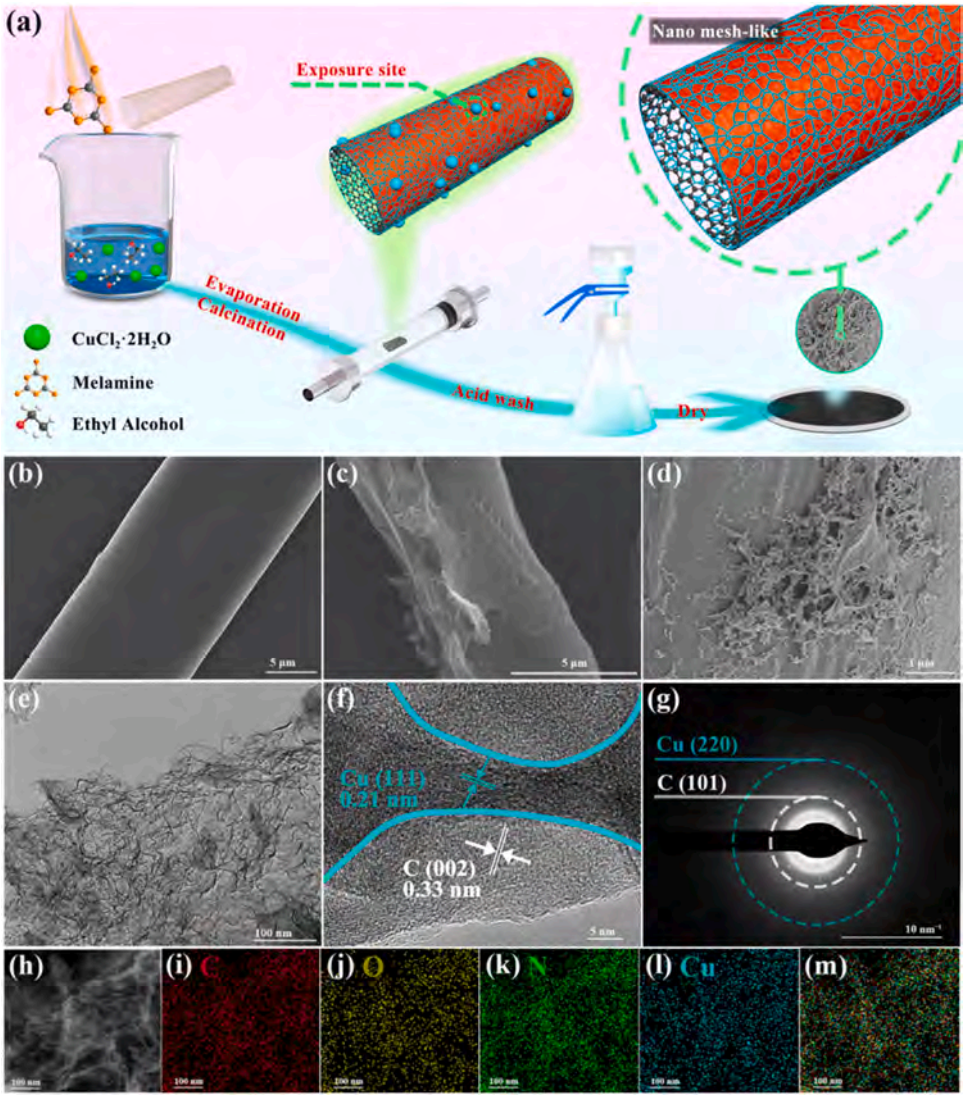

Fig. 1. (a) Synthesis of 0.6-Cu-N-KTC-KTC; (b-d) SEM images of KTC, N-KTC, and 0.6-Cu-N-KTC, (e, f) TEM and HR-TEM images of 0.6-Cu-N-KTC, (g) SAED pattern of 0.6-Cu-N-KTC, and (h-m) Elemental maps of 0.6-Cu-N-KTC.

2.5. Materials characterization

The surface microstructure of the materials was observed by SEM (Hitachi SU8600) and transmission electron microscopy (TEM, FEI Talos F200S). The microstructure was analyzed by X-ray diffraction (XRD, SmartLab), Raman scattering (RAM HR), and Fourier transform infrared spectroscopy (FTIR, NICOLET 380). The elemental composition and chemical states were determined by X-ray photoelectron spectrometry (XPS, ThermoFisher Nexsa), and radical ions were characterized by electron spin resonance (ESR, Bruker ESR JES-FA200).

3. Results and discussion

3.1. Characterization

As shown in Figs. 1b and S1, KTC has a smooth surface with distinct biomass-specific features. The tube diameter is between 2 and 10 μm [41]. After the introduction of melamine, N-KTC (Fig. 1c) shows a thin carbon layer on the carbon-tube. Compared to N-KTC, 0.6-Cu-N-KTC (Figs. 1d and S2) changes from a thin-layered to web-like morphology that is mediated by the nitrogen-bridging effects. The nitrogen-doped thin carbon layer provides anchoring sites for metallic Cu through Cu-N-C coordination, thereby preventing metallic Cu aggregation during carbonization. Subsequent acid etching removes the unstable Cu clusters while preserving the stable spider-web nanocopper framework. As shown in Fig. S3, the uniform fibrous structure on 0.6-Cu-KTC is formed by embedding Cu on the carbon-tube and acid. As shown in Fig. 1**e**, TEM reveals that the composite consists of nitrogen-doped carbon thin layers with the spider-web nanocopper structure. As show in Fig. 1**f**, distinct interplanar spacings measuring 0.21 nm and 0.33 nm are clearly resolved, which align with the characteristic (111) crystallographic orientation of metallic copper nano and the (002) basal plane of graphitic carbon, respectively [42]. The selected-area electron diffraction (SAED) pattern in Fig. 1**g** exhibits two concentric rings with diffraction radii of 0.128 nm and 0.235 nm from the (220) plane of nanocopper [43] and the (101) plane of the carbon matrix, respectively [44,36]. This spider-web nanocopper architecture has high porosity, and TEM-EDS **(Fig. h–m)** confirms homogeneous distributions of C, N, O, and Cu in the spider-web nanocopper structure.

As shown in the XRD spectrum in Fig. 2**a**, no diffraction peaks are observed from Cu or its compounds, perhaps due to multidirectional branching of the nano-web architecture and dispersed signals. The graphite (002) peak of the original carbon-tube KTC appears at 23.6°. After nitrogen doping, the diffraction peak of N-KTC shifts to 25.1°

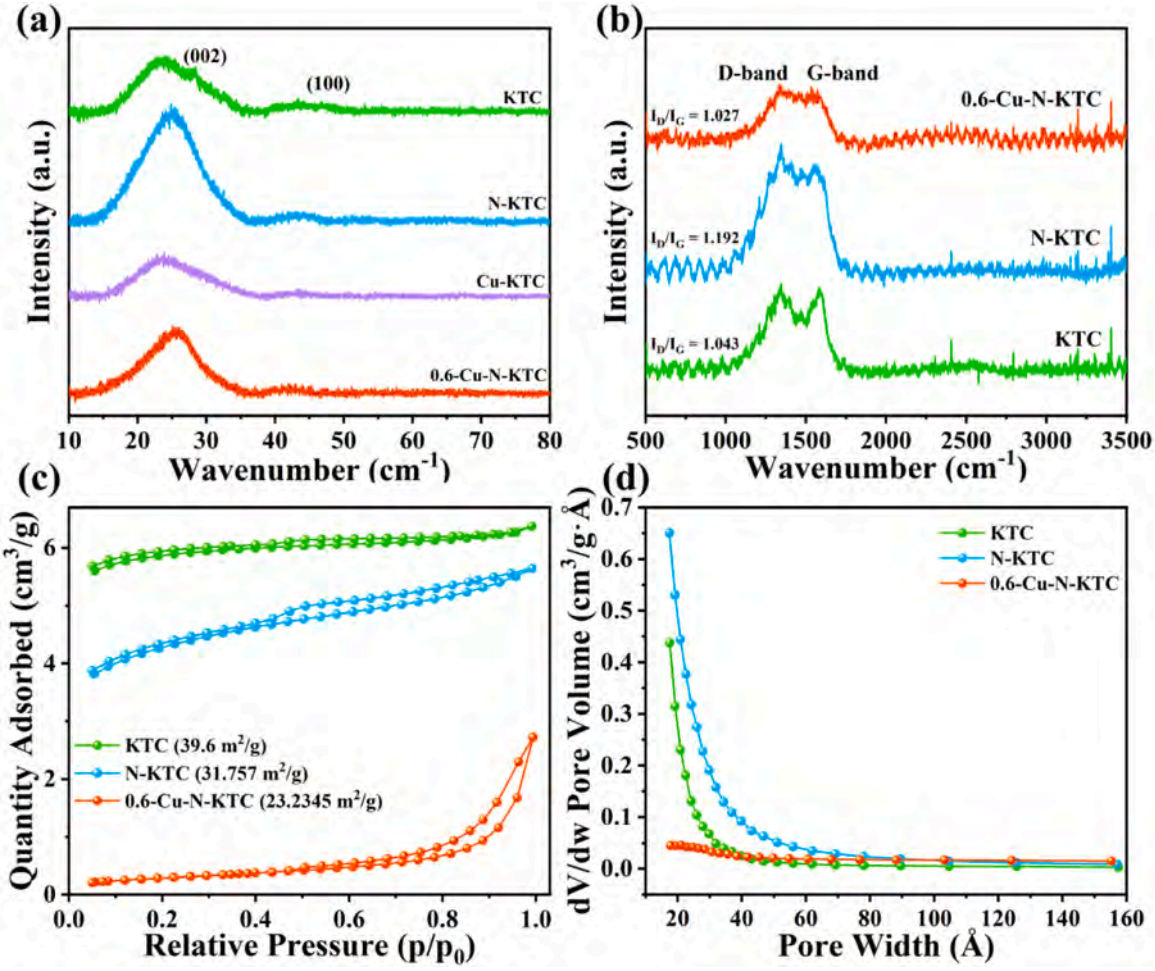

Fig. 2. (a) XRD patterns, (b) Raman scattering spectra, (c) N_2 adsorption-desorption isotherms, and (d) Pore size distributions.

because some carbon atoms in the carbon-tubes are replaced by nitrogen to form pyridine nitrogen and graphite nitrogen. This substitution expands the carbon layers, causing a blueshift in the diffraction peak. The more orderly lattice structure also produces higher signal intensity. The effect of Cu doping on carbon-tubes is minimal, as the diffraction peak of 0.6-Cu-KTC does not shift in spite of a small decrease [45]. This is likely because Cu reduces the crystallinity of the materials. The diffraction peak of graphite (002) from 0.6-Cu-N-KTC shows the same blueshift as N-KTC, while the diffraction peak of amorphous carbon (100) redshifts. Both peaks are weaker due to N and Cu doping.

As shown in Fig. S4, the FTIR spectrum exhibits a broad absorption band at 3450 cm^{-1}, which is ascribed to the stretching vibrations of hydroxyl (-OH) groups. The bands at 2916 cm^{-1} and 1662 cm^{-1} are assigned to C-H and C═C stretching vibrations, respectively [46]. while the band at 1387 cm^{-1} corresponds to the deformation vibration of carboxylate (COO-) groups. The peak at 1322 cm^{-1} is attributed to the stretching vibrations of C-N and C-O bonds [47,48]. No significant peak shifts are observed, indicating that the incorporated nitrogen species, primarily pyridinic nitrogen, exert a limited influence on C-N vibrations [49].Upon Cu incorporation, the formation of Cu-N coordination occurs, which induces only subtle changes in the peak positions but affects the intensity of specific bands. Furthermore, nitrogen doping suppresses the vibrations of functional groups such as C–H and C═O, leading to reduced intensity in N-KTC compared with the undoped counterpart. After Cu introduction, the formation of Cu–N structures results in a further decrease in intensity for 0.6-Cu-N-KTC relative to N-KTC. Meanwhile, the absence of notable peak shifts confirms the structural stability of the catalyst after Cu incorporation.

The Raman spectra presented in Fig. 2**b** exhibit two prominent vibrational signatures: a defect-related D band at 1347 cm^{-1} and a graphitic G band at 1570 cm^{-1}. The I_D/I_G ratio of KTC is 1.043. After the introduction of nitrogen, the I_D/I_G ratio of N-KTC increases to 1.192, indicating the formation of more defects, whereas after copper incorporation, the I_D/I_G ratio of 0.6-Cu-N-KTC (1.027) decreases, suggesting that Cu enhances graphitization.

As shown in Fig. 2**c**, the nitrogen adsorption-desorption isotherms of KTC, N-KTC, and 0.6-Cu-N-KTC samples display typical Type IV characteristics with pronounced H3-type hysteresis loops. The hysteresis loop of 0.6-Cu-N-KTC is the most pronounced due to the multilayered structure with microporous or mesoporous characteristics, consistent with TEM [50]. The pore size distribution in Fig. 2**d** reveals predominantly mesopores formed by the acid treatment after Cu incorporation. After Cu and N loading, the surface area decreases because they occupy some of the original carbon-tube pores. Notably, The pristine KTC contains negligible nitrogen species, suggesting that the intrinsic substrate contributes little to PMS activation. Its relatively high specific surface area and mesoporous structure mainly facilitate pollutant adsorption rather than direct catalytic activation. Upon nitrogen doping and Cu incorporation, the surface area and porosity decrease slightly; however, the catalytic activity significantly increases, confirming that the enhanced performance arises from the formation of abundant Cu-N-C active sites and improved electron transfer pathways rather than from the pristine carbon structure itself. Overall, 0.6-Cu-N-KTC favors the adsorption of pollutants and PMS.

As shown in Fig. 3**a**, the XPS C 1 *s* peak at 285.9 eV contains C-O and C-N information. After nitrogen doping, the peak area increases because

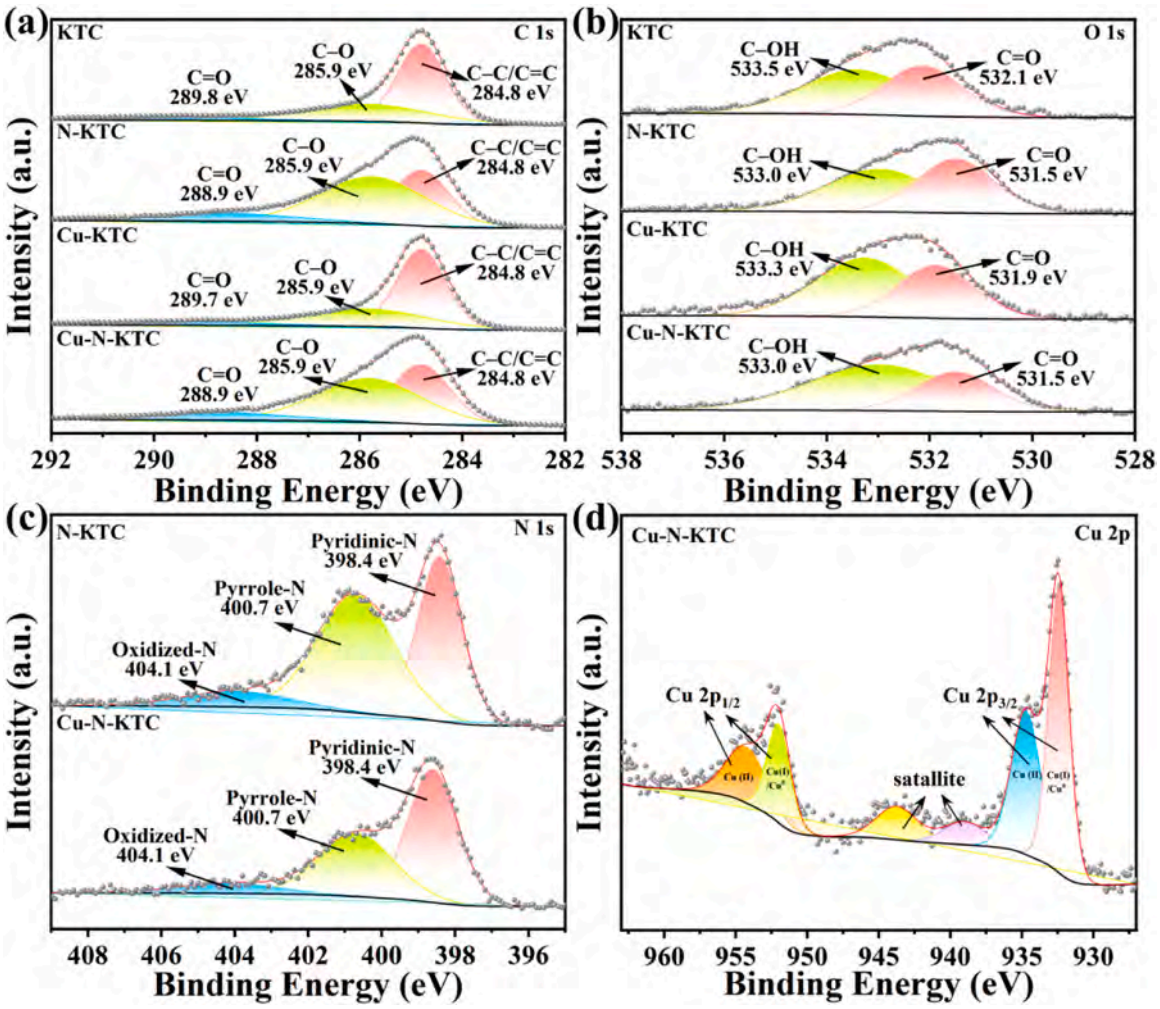

Fig. 3. XPS spectra: (a) C 1 *s*, (b) O 1 *s*, (c) N 1 *s*, and (d) Cu 2*p*.

nitrogen substitutes some carbon atoms. This substitution also decreases the peak at 284.8 eV of C-C/C═C, which is related to the formation of C-N bonds [51]. The C-N bonds draw electrons from C toward N to reduce the electron density of C and lower the binding energy of C═O, causing the peak at 289.8 eV to shift to 288.9 eV. A similar trend is observed from the O 1 *s* spectrum (Fig. 3**b**), in which the binding energy of the C═O peak decreases after N introduction. In addition, oxygen in adsorbed water shows a slight decrease in the binding energy. As shown in Fig. 3**c**, after the introduction of Cu, the peak of pyrrole-N decreases compared to N-KTC due to electron donation from Cu atoms through the *d*-orbitals to the *p*-orbitals of pyrrole-N or the alteration of pyrrole-N's electron density *via* Cu-N coordination.

As shown in the Cu 2*p* spectrum Fig. 3**d**, Cu is detected only from 0.6-Cu-N-KTC due to the acid treatment. Cu atoms adsorb onto the carbon nanotubes mainly physically and through minor Cu-C coordination. They are easily removed by acid washing, and no residual Cu can be detected. The two strong peaks at 932.5 eV and 952.1 eV are Cu^0/Cu(I) [52], with the 932.5 eV peak related to Cu-N and that at 939.1 eV attributed to Cu(I) (Cu_2O) [53]. The peaks at 954.6 eV, 943.7 eV, and 934.7 eV are generally associated with Cu(II), which likely arises from the formation of CuO as a result of Cu interacting with oxygen adsorbed on the carbon nanotube. The Cu(I) and Cu0 peaks of both Cu $2p_{1/2}$ and Cu $2p_{3/2}$ are more intense than Cu(II), confirming that Cu exists predominantly in a reduced state. Nitrogen is in the form of pyridine nitrogen and pyrrole nitrogen with Cu forming a Cu-N with pyrrole nitrogen for active sites. N-doping encapsulates Cu to mitigate leaching and enhance the stability.

3.2. Catalytic degradation

The degradation efficiency of TCH as a model pollutant is evaluated under different conditions (KTC, N-KTC, 0.6-Cu-KTC, and 0.6-Cu-N-KTC) together with PMS activation. As shown in Fig. 4**a**, the degradation efficiency of KTC/PMS, N-KTC/PMS, and 0.6-Cu-KTC/PMS is comparable to that of PMS alone. As shown in Fig. S5, in the absence of PMS, neither KTC nor the N or Cu doped material will cause degradation of TCH. However, when Cu and N are introduced together, the catalytic efficiency of 0.6-Cu-N-KTC/PMS increases. The first-order rate constant (K_{OBS}) of 0.6-Cu-N-KTC/PMS (0.0726 min^{-1}) is 3.17, 2.77, and 3.12 times higher than those of KTC (0.0229 min^{-1}), N-KTC (0.0262 min^{-1}), and 0.6-Cu-KTC (0.0233 min^{-1}), respectively (Fig. S6a).

To verify that Cu sites are the primary active sites, experiments are conducted based on the ability of EDTA-2Na to form stable complexes with metal sites. As shown in Fig. S7a, the degradation rate decreases gradually with EDTA-2Na concentrations. Similarly, KSCN is used to capture Cu sites (Fig. S7b), and the same conclusion is reached to assert the key role of Cu sites in the degradation process. After establishing Cu and N co-doping as the target, materials with samples with different Cu concentrations are prepared (Fig. 4**b**). 0.6-Cu-N-KTC exhibits the best TCH degradation efficiency within 30 min. When the amount is less than 0.6, there are insufficient active sites, but when it exceeds 0.6, Cu aggregation reduces the utilization of active sites resulting in lowering catalytic efficiency [54].

Metal leaching occurs, and the process is monitored by ICP-OES to determine the amount of Cu released by 0.6-Cu-N-KTC. Solutions with

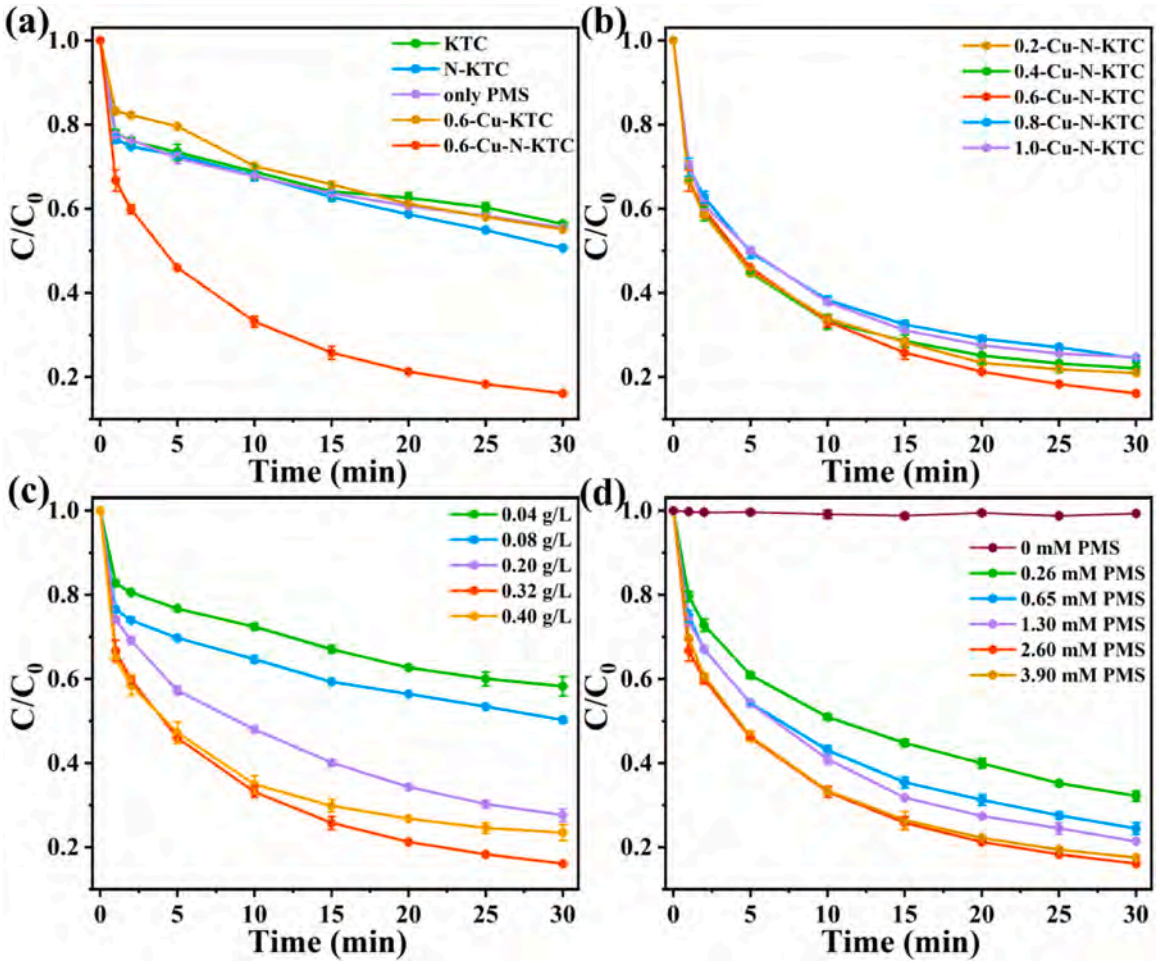

Fig. 4. (a) Degradation efficiency of TCH in different systems, (b) Effects of Cu concentration on TCH degradation, (c) Effects of the catalyst dosage on TCH degradation, and (d) Effects of PMS dosage on TCH degradation.

the same concentration are prepared, and as shown in Fig. S8, the degradation rate of the leachate is consistent with that of the Cu ion solution, proving that the degradation effect arises from Cu ions. As shown in Fig. 4**c**, when the dosage of 0.6-Cu-N-KTC is increased from 0.04 g/L to 0.32 g/L, the degradation efficiency of TCH goes up, and K_{OBS} increases from 0.0217 min^{-1} to 0.0726 min^{-1} (Fig. S6c). However, when the catalyst dosage is further increased to 0.40 g/L, the catalytic efficiency after 10 min decreases because of side reactions and blocking of active sites. As shown in Fig. 4**d**, the degradation efficiency of TCH increases with the amount of PMS, reaching a maximum at 2.60 mmol/L because more PMS molecules are activated by increasing contact and reactive species for degradation.

After reducing the TCH concentration, the degradation performance improved as expected (Fig. S9). The value of K shows a clear increasing pattern (Fig. S6e). When the pollutant concentration was at 5 mg/L, complete degradation was achieved within 25 min. Comparing the K_{OBS} values under these conditions (Fig. S6), the influence of the four parameters is ranked as follows: [catalyst dosage] > [PMS dosage] > [Cu loading] > [TCH concentration]. It can also be inferred that the activation of active sites on 0.6-Cu-N-KTC after PMS adsorption is the key factor.

In natural water, in addition to pollutants such as antibiotics, anions like Cl^-, PO_4^{3-}, NO_3^-, and HCO_3^- as well as humic acid (HA) are present, and they influence the degradation of the 0.6-Cu-N-KTC/PMS system [55]. As shown in Fig. 5**a**, the addition of 2 mmol/L PO_4^{3-}, NO_3^-, and HCO_3^- does not significantly inhibit the degradation of TCH. It can be observed that the addition of Cl^- significantly reduces the degradation performance. This might be because Cl^- reacts with PMS to form HOCl, and HOCl is a relatively weak type of reactive oxygen species [56]. Among them, the inhibitory effect of PO_4^{3-} was more significant, as phosphate is typically considered a scavenger of ·OH to reduce the concentration of active species and suppress TCH degradation. HCO_3^- can react with $SO_4^{\bullet-}$ to form $HCO_3^{\bullet}$ and CO_3^{2-}, while NO_3^- can react with $SO_4^{\bullet-}$ to generate nitrate radicals. These newly formed radicals are less reactive and contribute minimally to the degradation of TCH. They also consume reactive species in the process and decrease the degradation efficiency.

The degradation performance of 0.6-Cu-N-KTC/PMS decreases after the addition of humic acid (HA) because HA competes with TCH for active sites and reactive species. The degradation performance is assessed in real water samples, as shown in Fig. 5**b**. In both seawater and river water, degradation is near maximum within 1 min. This may be because the alkaline condition of water enhances TCH degradation. In contrast, tap water, which may contain natural organic matter (NOM), likely competes with PMS to consume reactive species and mitigate TCH degradation. In practice, wastewater treatment often encompasses processes in which the temperature exceeds 40 °C. Therefore, the degradation performance of 0.6-Cu-N-KTC/PMS is evaluated at different temperatures. As shown in Fig. 5**c**, as the temperature increases from 23 °C to 45 °C, the degradation properties improve. According to the Arrhenius mechanism, a higher temperature enhances the kinetic energy of the reactants and expedites the reaction between the catalyst and tetracycline hydrochloride (TCH). Moreover, the higher kinetic energy reduces the self-inhibition effect of PMS to improve the degradation efficiency.

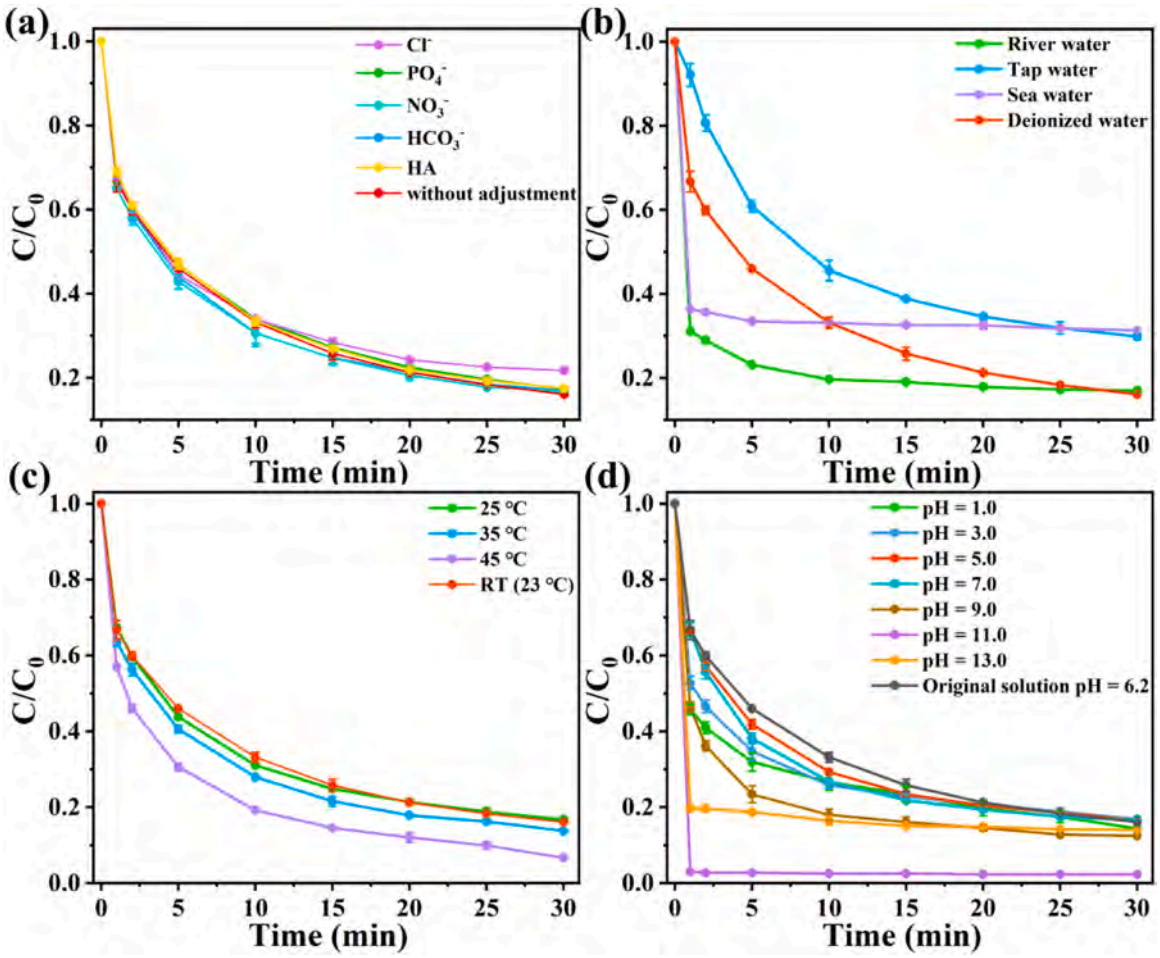

Fig. 5. (a) Effects of anions on TCH degradation [anions] = 2.0 mmol/L; (b) Effects of water quality on TCH degradation; (c) Effects of temperature on TCH degradation; (d) Effects of pH on TCH degradation. Conditions: [Cat.] = 0.32 g/L, [PMS] = 0.26 mmol/L, [TCH] = 30 mg/L, initial pH = 6.2 (without adjustment), and T = 23°C. The number of repeated experiments is two.

The effects of pH are studied. The initial pH of the 30 mg/L TCH solution is 6.2, and the pH is adjusted by adding KOH or HCl. Fig. 5**d** shows that 0.6-Cu-N-KTC/PMS has excellent degradation efficiency over a broad pH range from 1 to 13. Within the pH range of 1.0–6.2, the degradation rate increases as the pH decreases, while the endpoint of degradation remains relatively unchanged due to under acidic conditions, Cu(I) can stably form, accelerating electron transfer and increasing the rate of ROS production and HSO_5^- becomes the dominant species to rapidly generate more $SO_4^{\bullet-}$ and accelerate the reaction. This might be because TCH gradually undergoes protonation, transforming into a negatively charged form. The electrostatic attraction between this negatively charged form and the positively charged Cu active center increases, thereby facilitating the reaction. When the base is in excess (pH = 13), the excess OH^- reacts with HSO_5^-, reducing the utilization rate of PMS. As a result, the reaction terminates shortly after PMS rapidly degrades.

To investigate the electric field between the material surface and solution, the zeta potentials are measured, as shown in Fig. S10. At the pH of 11, the moderate negative surface charge on the material enhances PMS activation to allow rapid activation and nearly complete degradation within 1 min. At the pH of 13, the higher negative charge strengthens the electrostatic repulsion between the material and TCH and reduces the degradation efficiency. When the surface potential is positive, TCH, primarily existing in a negatively charged state, experiences strong electrostatic attraction to the positively charged surface for better adsorption degradation. In summary, the 0.6-Cu-N-KTC/PMS system exhibits outstanding TCH degradation performance over a broad pH range of 1–13.

3.3. Active species and degradation mechanism of 0.6-Cu-N-KTC/PMS

By means of radical trapping experiments and ESR, the active species in the 0.6-Cu-N-KTC/PMS system are determined. With regard to •OH, the reaction rate with MeOH (9.7×10^8 M^{-1} s^{-1}) is similar to that with TBA ($3.8–7.6 \times 10^8$ M^{-1} s^{-1}) [57]. In contrast, as for $SO_4^{\bullet-}$, the reaction rate with MeOH ($0.32–1.1 \times 10^7$ M^{-1} s^{-1}) is significantly higher than that with TBA ($4–9.5 \times 10^5$ M^{-1} s^{-1}). As shown in Fig. 6**a**, the degradation rate of TCH is influenced more by the addition of MeOH than TBA, indicating that •OH contributes minimally to the degradation of TCH. The more pronounced suppression of degradation by MeOH further confirms the key role of $SO_4^{\bullet-}$. The effects of MeOH concentrations on TCH degradation are monitored (Fig. S11). The degradation efficiency of TCH diminishes from 84 % to 58 % with elevated concentrations of MeOH. The poor quenching effect of DMSO also supports the conclusion that •OH is not the primary active species in the system. ESR (Fig. 6**c**) shows that the peak intensity of $SO_4^{\bullet-}$ and •OH from 0.6-Cu-N-KTC/PMS increases with time, corroborating that PMS is activated and $SO_4^{\bullet-}$ and •OH being intermediate active species. However, they do not fully participate in the degradation of TCH. The degradation rate of TCH decreases by 14.6 % upon quenching of $\bullet O_2^-$ by p-BQ (1.0×10^9 M^{-1} s^{-1}), indicating that $\bullet O_2^-$ plays a significant role, in line with ESR (Fig. 6**d**), which shows that the intensity of $\bullet O_2^-$ increases with time.

In the non-radical pathway, the quenching of $^1O_2$ by FFA ($5.3–7.0 \times 10^8$ M^{-1} s^{-1}) and L-Trp ($0.86–1.1 \times 10^9$ M^{-1} s^{-1}) results in a

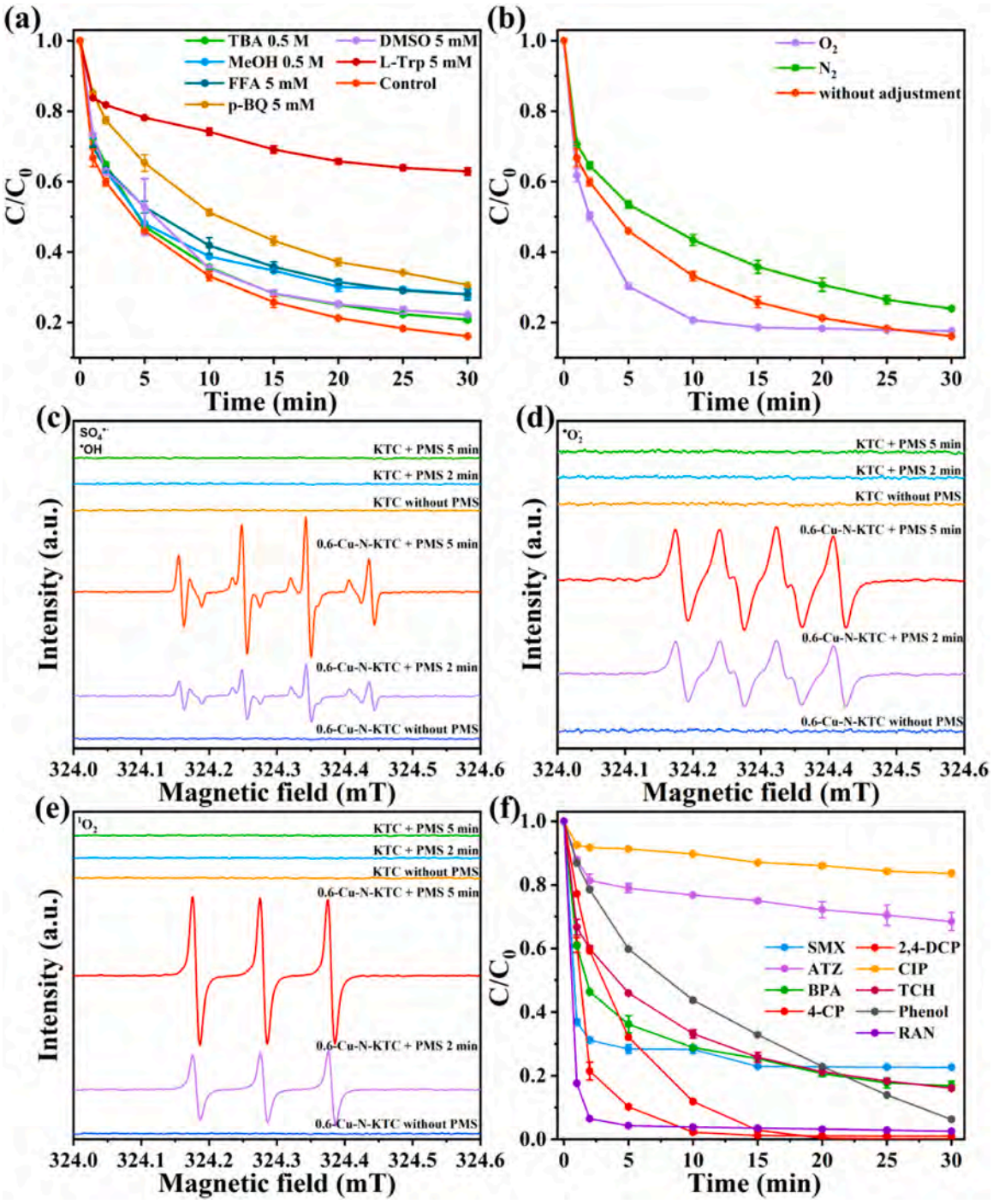

Fig. 6. (a) TCH degradation of 0.6-Cu-N-KTC in the presence of scavengers; (b) TCH degradation of 0.6-Cu-N-KTC in different atmospheres; EPR spectra of (c) •OH and $SO_4^{\bullet-}$, (d) $\bullet O_2^-$ and (e) $^1O_2$ in different systems; (f) Degradation effects of different contaminants. Conditions: [Cat.] = 0.32 g/L, [PMS] = 0.26 mmol/L, [TCH] = 30 mg/L, initial pH = 6.2 (without adjustment), and T = 23 ℃. The number of repeated experiments is two.

degradation rate decrease of 12 % and 46.8 %, respectively. These findings indicate that $^1O_2$ is the primary active species consistent with ESR (Fig. 6**e**). The generation of $^1O_2$ is likely associated with PMS activation and dissolved oxygen. To further investigate the influence of the gas atmosphere on degradation, different gas environments are assessed. The N-bridging effect enhances the electron density around Cu active centers via Cu-N coordination. This facilitates rapid electron shuttling between Cu(I)/Cu(II) during PMS activation, accelerating both radical ($SO_4^{\bullet-}$, $\bullet O_2^-$) and non-radical ($^1O_2$) pathways. As shown in Fig. 6**b**), the degradation rate goes under in the O_2 atmosphere, suggesting that dissolved oxygen plays important roles in generating $\bullet O_2^-$ and $^1O_2$ in the degradation process. In contrast, in the N_2 atmosphere, the degradation rate decreases slightly by 8 %. The results suggest that dissolved oxygen facilitates the generation of $^1O_2$, but it is not the exclusive pathway for its production.

No signals are detected from free radicals or non-radical species in the ESR spectra of the KTC/PMS system and that without PMS, consistent with the experimental results. Cu and N as active sites promote PMS activation and pollutant degradation. To further evaluate the degradation of various pollutants such as ATZ, CIP, SMX, 2,4-DCP, BPA, 4-CP, phenol, and RAN, experiments are conducted, and the results are shown in Fig. 6**f**. The catalyst exhibited efficient degradation of various

organic pollutants (The K value is shown in Fig. S6f.). 2,4-DCP and 4-CP show the best degradation results. Both molecules contain chlorine making them more reactive in oxidation. Chlorine promotes the generation of free radicals and enhances the reactivity by interacting with metals on the catalyst. Chlorine also increases the affinity of the molecules to reactive oxygen species to improve the degradation efficiency. The furan structure in the RAN molecules with oxygen atoms reduces the electron density due to the electronegativity of oxygen, making the molecule more susceptible to attack and degradation by active species. BPA, phenol, and other relatively hydrophilic molecules adsorb easily onto the surface and react with the catalyst. In contrast, ATZ and CIP, being more hydrophobic, cannot adsorb as easily, leading to poor contact with the catalyst and reduced catalytic efficiency.

Although $^1O_2$ and $\bullet O_2^-$ play key roles in the degradation of TCH, the reaction does not cease in the presence of quenchers, consequently prompting an investigation into the electronic pathway of TCH degradation. Upon activation, PMS generates electrons, and TCH, which contains a π-electron system, provides a rich electron density, making the generated electrons more readily available to directly attack TCH. This allows the system to degrade TCH even in the absence of free radicals. Subsequently, electrochemical tests are conducted to elucidate the electron transfer pathways.

The i-t curve is used to monitor charge transfer, as shown in Fig. 7**a**. PMS is added at 100 s, and a noticeable current is observed, indicating that PMS reacts with the active sites on the surface. When TCH is introduced at 200 s, the current becomes more pronounced as the synergistic effect between TCH and PMS enhances electron transfer. The LSV curve in Fig. 7**b** shows the current densities of different systems. In the absence of additives, the current is relatively small, but when PMS or TCH is added separately, the current increases rapidly, indicating that PMS is activated individually and that TCH interacts with the material. However, with low reaction activity, it does not drive degradation. However, when both PMS and TCH are added together, the current increases. At lower potentials, 0.6-Cu-N-KTC exhibits a more negative current, indicating that the combined action of PMS and TCH promotes the electrochemical reaction and produces a more negative current. As the potential increases, the current stabilizes gradually, implying that the redox reaction reaches a saturated potential and the current reaches a steady state. This is consistent with the i-t curve. The EIS results in Fig. 7**c** show that 0.6-Cu-N-KTC exhibits a smaller semicircle radius than KTC, indicating that Cu and N doping enhances electron transfer and facilitates faster electron migration to the active sites for TCH degradation. The equivalent circuit consists of R_s (intrinsic resistance), Rct (charge transfer resistance), and a constant phase element (CPE), with the low-frequency tail mainly attributed to Warburg impedance.

3.4. Degradation pathways

To investigate the degradation pathway of 0.6-Cu-N-KTC/PMS, LC-MS is conducted to identify the intermediate products, as shown in Fig. 8. Initially, TCH undergoes hydrolysis in water to form TC P0 ($m/z = 445.1$), which is subsequently degraded in two possible pathways. In Pathway I, the two methyl groups attached to nitrogen are sequentially demethylated. The methyl group farthest from the ring structure is removed first to form P1 ($m/z = 432.9$), followed by the removal of the second methyl group. At the same time, $SO_4^{\bullet-}$ and $\bullet O_2^-$ attack the amide group, leading to its removal and formation of P2 ($m/z = 374.1$). The C═C and aromatic ring structures in P2 are oxidatively cleaved by $^1O_2$ to form P3 ($m/z = 305.1$), P4 ($m/z = 301.1$), and P5 ($m/z = 261.1$), which are open-ring compounds. In Pathway II, the methyl group attached to the amino group of TC is removed first to possibly form a nitrogen oxide intermediate. After the deamination reaction, a carbonyl group (P6, $m/z = 414.9$) is formed. In the presence of $SO_4^{\bullet-}$, $\bullet O_2^-$, and $^1O_2$, methyl and hydroxyl groups are further removed to reduce the molecular energy and increase the stability, leading to the formation of P7 ($m/z = 384.9$). Subsequently, as in Pathway I, the open-ring reaction produces P8 ($m/z = 216.9$), P9 ($m/z = 137.0$), and other compounds. Finally, these intermediate products are decomposed into small molecules like CO_2, and H_2O.

3.5. Cyclic stability and repeatability

Cyclic stability and renewability are important criteria for catalytic materials in practical applications. Here, after use, the catalyst is collected, washed by filtration with 250 mL of deionized water, and dried to obtain the recycled material for repeated testing (Fig. S12a). After four cycles, the performance decreases by only 17 %. This phenomenon may be due to the oxidation or passivation of Cu sites during degradation or the blockage of pores by degradation products or reaction intermediates, which reduce the effective contact area for catalytic reactions and diminish the catalytic performance. Fortunately, this situation can be reversed. The recycled material is collected, dried, and heated in a nitrogen atmosphere at 10 °C/min to 400°C and held for 1 h. The performance is found to recover by 100 % on account of the removal of impurities from the Cu surface and in the pores during secondary calcination, which also reduces the oxidized Cu sites. Furthermore, calcination likely promotes the dispersion or reorganization of copper particles. XRD confirms the structural stability of the materials before and after cycling and regeneration (Fig. S12b) and discloses that 0.6-Cu-N-KTC maintains good stability and recyclability.

The degradation mechanism of 0.6-Cu-N-KTC and the changes occurring during cycling and regeneration are investigated by XPS. The C 1*s* spectrum (Fig. S13a) reveals a noticeable shift in the peak near 288.9 eV, indicating a smaller binding energy after cycling. This may be

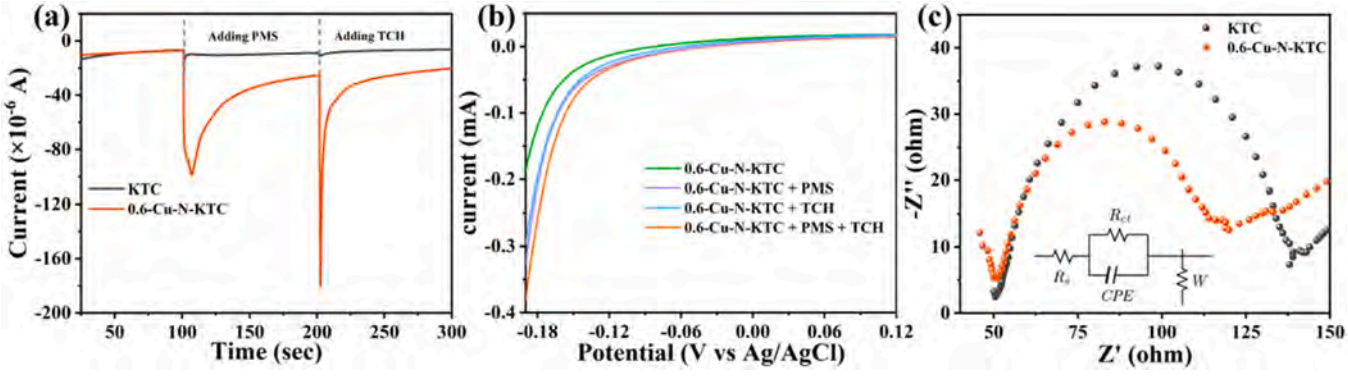

Fig. 7. (a) i-t curves obtained at 0.0 V vs. Ag/AgCl (0.5 mol/L Na_2SO_4); (b) LSV curves obtained under different conditions; (c) EIS spectra of KTC and 0.6-Cu-N-KTC loaded on the FTO glass electrodes.

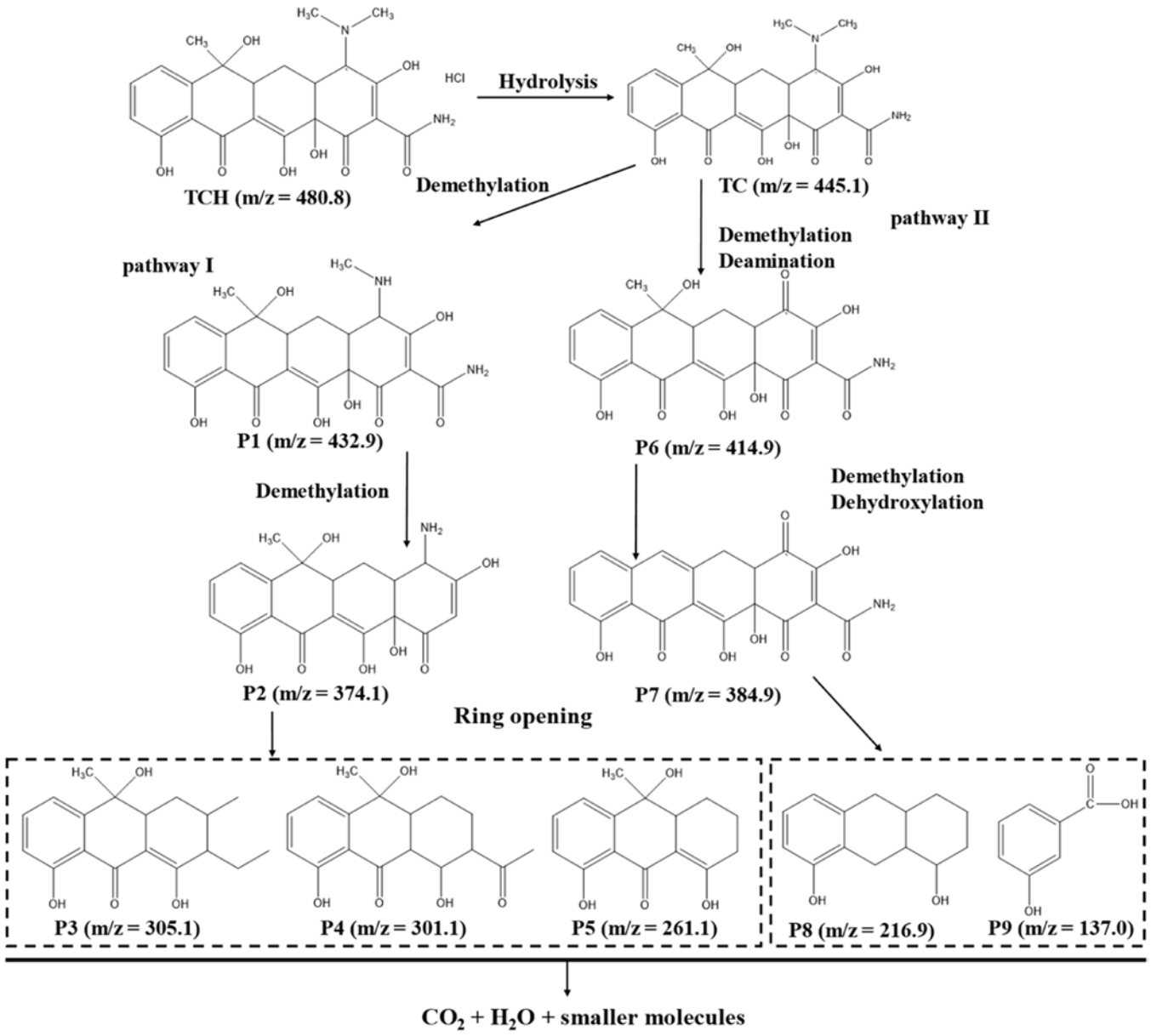

Fig. 8. (a) Postulated degradation pathways of TCH by 0.6-Cu-N-KTC/PMS.

due to the conversion of carboxyl (C═O) to a less catalytically active ketone functional group. The secondary calcination process likely restores the carboxyl group and facilitates the recovery of activity. In the O 1 *s* spectrum (Fig. S13b), the peak of carboxyl oxygen at 513.5 eV shifts to 531.7 eV, corresponding to ketone oxygen after cycling. The peak between 532.5–533.5 eV represents oxygen in adsorbed water on the surface, which remains unchanged during the experiment. The N 1 *s* spectrum (Fig. S13c) shows that the peak between 403.5–404.5 eV, which corresponds to Cu-N, increases in intensity and exhibits a higher binding energy after regeneration, likely due to the rearrangement of copper particles. In the Cu 2*p* spectrum (Fig. S13d), both the Cu $2p_{1/2}$ and Cu $2p_{3/2}$ peaks show a higher intensity of Cu(II) after cycling, while the intensity of the Cu(I) peak increases after regeneration. This suggests that Cu is the primary active site and that the catalytic activation reaction is driven by the transition from Cu(I) to Cu(II). These results also point out that 0.6-Cu-N-KTC has excellent cycling stability and regenerative properties.

3.6. TOC analysis and biological toxicity

To verify whether TCH can be oxidized into inorganic compounds (H_2O, CO_2), the total organic carbon (TOC) is determined, as shown in Fig. 9. The oxidation capacity of the KTC/PMS system is significantly lower than that of the 0.6-Cu-N-KTC/PMS system, as manifested by TOC removal rates of 26.2 % and 53.7 %, respectively, after 100 min. The results align with the observation by LC-MS. In the Fenton reaction system, the Rhodamine B (RhB) solution undergoes a noticeable color change from red to transparent during degradation by 0.6-Cu-N-KTC, indicating that the pollutant is rapidly oxidized and degraded boding well for industrial applications.

To assess the biological toxicity of the materials, degradation solutions from different time intervals are mixed with Escherichia coli suspensions and cultured on agar plates, as shown in Fig. 10**a-h**. Colonies appear after 5 min, and the number of colonies increases with time. After 30 min, the colony count is nearly the same as that of the original E. coli suspension. To understand the inactivation mechanism of the 0.6-Cu-N-KTC/PMS/TCH system against E. coli, SEM is performed on the E.

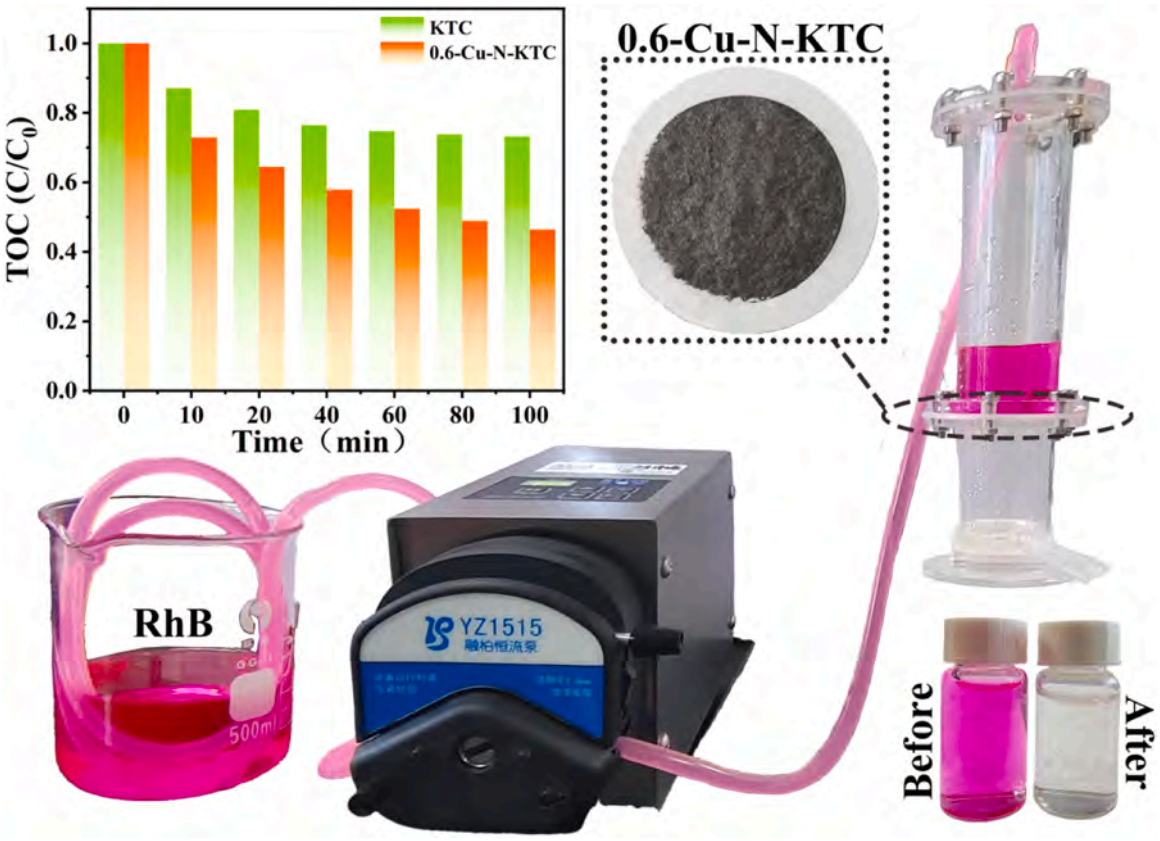

Fig. 9. TOC removal during TCH degradation by 0.6-Cu-N-KTC/PMS and RhB degradation of 0.6-Cu-N-KTC use a pump setup.

coli cells treated with the degradation solution for 5 min and 15 min in conjunction with untreated E. coli. Fig. 10**i and j** depict the SEM images of untreated E. coli and E. coli after 15-min degradation. After 15-min degradation, there is minimal impact on the E. coli cell structure. Fig. 10**k-n** illustrate the damaged regions of E. coli after exposure to the degradation solution. Both the 5-min and 10-min degradation solutions cause cell rupture as ROS generated by PMS disrupts the lipid bilayer and changes the membrane permeability. A comparison of the deformed E. coli treated with the 5-min and 15-min degradation solutions reveals that the degree of deformation decreases with degradation time. This is likely due to the reduced inhibitory effect of TCH on protein synthesis as its concentration decreases over time. To eliminate the influence of PMS on E. coli, a 2.60 mmol/L PMS solution is prepared as a control, and negligible impact is observed [58].

3.7. Degradation mechanism

Based on the above experimental results, a degradation mechanism is proposed for the 0.6-Cu-N-KTC/PMS/TCH system. As indicated by ESR, the catalyst activates PMS to generate •OH, $\bullet O_2^-$, $SO_4^{\bullet -}$, and $^1O_2$ to degrade TCH. The degradation mechanism is illustrated in Fig. 11. The spider-web structure facilitates the adsorption of pollutants and PMS. XPS shows that Cu primarily exists in its reduced states (Cu^0 and Cu(I)), which are oxidized to Cu(II) during activation, accompanied by the generation of large amounts of $SO_4^{\bullet -}$ and •OH (Eqs. 1–3). Subsequently, Cu(II) reacts with PMS to produce $SO_5^{\bullet -}$ (Eq. 4), which interacts with H_2O to generate $^1O_2$ (Eq. 5). This is considered the primary pathway for $^1O_2$ formation. Moreover, the nitrogen-bridging not only stabilizes the spider-web-like Cu nanowires but also tunes the local electronic environment by forming Cu-N-C sites, which act as highly efficient redox centers for PMS activation. This bridging effect promotes the Cu(I)/Cu(II) redox cycling and the generation of singlet oxygen ($^1O_2$) through electron-mediated pathways.

The gas atmosphere experiments demonstrate that dissolved oxygen (O_2) enhances degradation. This is likely because O_2 can oxidize Cu(I) to produce $\bullet O_2^-$ and Cu(II) (Eq. 6). The generated $\bullet O_2^-$ subsequently reacts with Cu(II) to regenerate Cu(I) and produce $^1O_2$ (Eq. 7). This Cu redox cycle utilizes dissolved oxygen in water to enhance the long-term stability and recyclability of the catalyst. Owing to the high initial concentration of PMS in the solution, PMS may undergo self-dissociation to produce SO_5^{2-} (Eq. 8). Under alkaline conditions, SO_5^{2-} can react with PMS to form $^1O_2$ (Eq. 9) to explain the rapid reaction kinetics.

Electrochemical tests confirm that electron transfer occurs during the catalytic reaction, in which electrons react with O_2 to form $\bullet O_2^-$ (Eq. 10). $\bullet O_2^-$ can react with •OH or H_2O to produce $^1O_2$ (Eqs. 11–12). However, these reactions are typically challenging due to the weak oxidative nature of $\bullet O_2^-$ and the distinct conditions required for its coexistence with $^1O_2$. These reactions often require specific catalytic conditions, such as the presence of transition metals, alkaline environments, or irradiation, to proceed efficiently. Furthermore, the porous channel structure and the surface-rich oxygen-containing functional groups (e.g., C═O) facilitate the catalytic degradation of TCH through PMS activation on its surface. This ultimately leads to the breakdown of TCH into smaller molecules, such as CO_2 and H_2O, to complete the degradation process.

$$Cu^0 + HSO_5^- \rightarrow Cu(I) + SO_4^{\bullet -} + OH^- \quad (1)$$

$$Cu(I) + HSO_5^- \rightarrow Cu(II) + SO_4^{\bullet -} + OH^- \quad (2)$$

$$Cu(I) + HSO_5^- \rightarrow Cu(II) + SO_4^{2-} + \bullet OH \quad (3)$$

$$Cu(II) + HSO_5^- \rightarrow Cu(I) + SO_5^{\bullet -} + H^+ \quad (4)$$

$$4SO_5^{\bullet -} + 2H_2O \rightarrow 4SO_4^- + 3^1O_2 + 4H^- \quad (5)$$

$$O_2 + Cu(I) \rightarrow Cu(II) + \bullet O_2^- \quad (6)$$

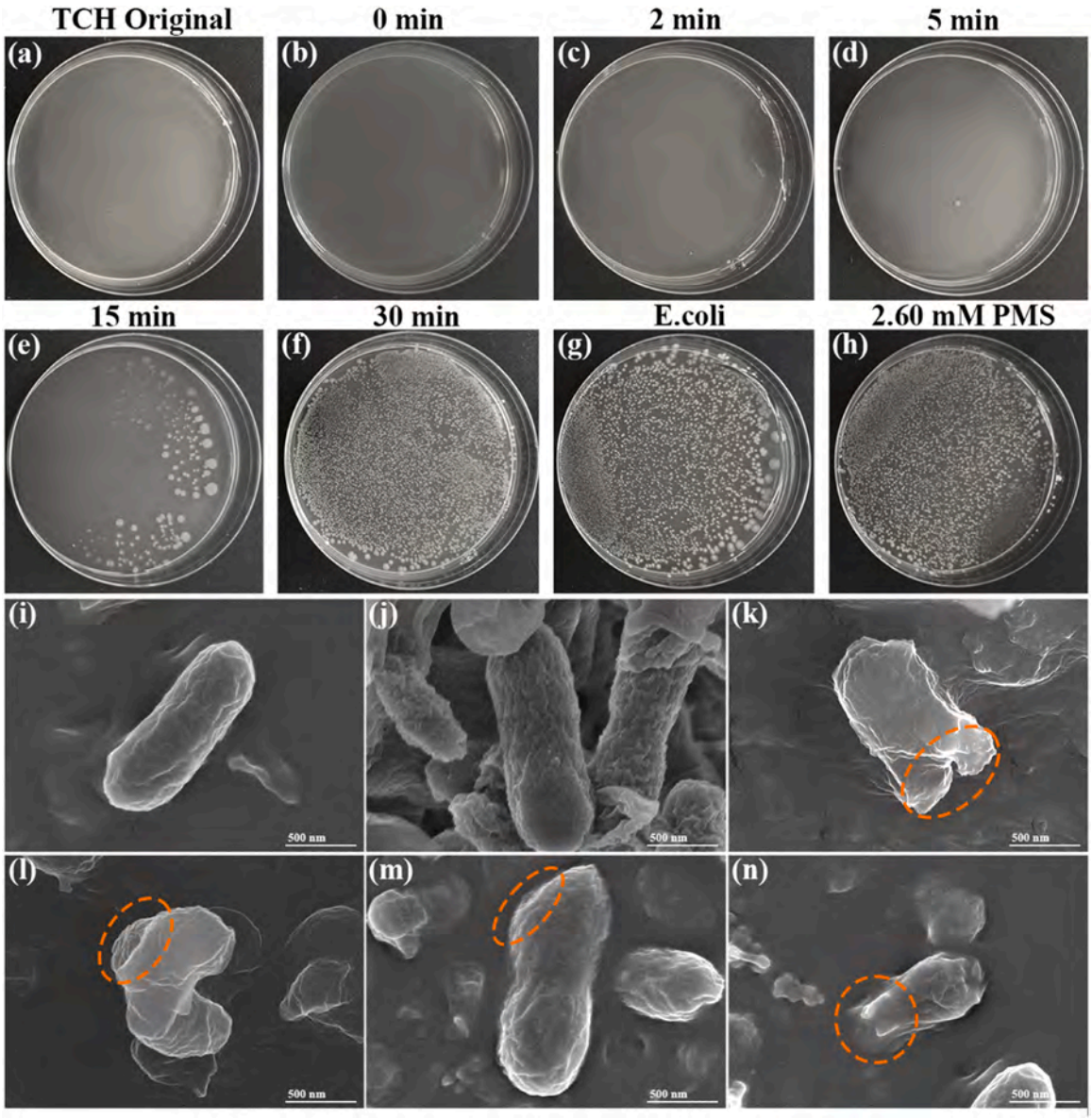

Fig. 10. (a-h) E. coli growth in 30 mg/L tetracycline hydrochloride culture and different, degradation solutions for 0 min, 2 min, 5 min, 15 min, and 30 min, bacterial stock culture, and 2.60 mmol/L PMS solution culture; SEM images of healthy E. coli originating from (i) E. coli stock solution and (j) 15-min degradation solution; Damaged E. coli originating of (k, l) 5-min and (m, n) 15-min degradation solutions.

$$\bullet O_2^- + Cu(II) \rightarrow Cu(I) + {}^1O_2 \quad (7)$$

$$HSO_5^- \rightarrow SO_5^{2-} + 2H^+ \quad (8)$$

$$HSO_5^- + SO_5^{2-} \rightarrow HSO_4^- + SO_4^{2-} + {}^1O_2 \quad (9)$$

$$O_2 + e^- \rightarrow \bullet O_2^- \quad (10)$$

$$\bullet O_2^- + \bullet OH \rightarrow {}^1O_2 + OH^- \quad (11)$$

$$2\bullet O_2^- + 2H_2O \rightarrow 2{}^1O_2 + 2OH^- + H_2O_2 \quad (12)$$

4. Conclusions

A nitrogen-bridged spider-web nanocopper wire composite is anchored on kapok-derived carbon (0.6-Cu-N-KTC) to form an efficient catalyst for peroxymonosulfate (PMS) activation and organic pollutant degradation. The unique architecture of the catalyst, featuring ultrathin nitrogen-doped carbon layers interwoven with highly dispersed Cu nanowires, enhances PMS activation *via* optimized electron transfer and abundant Cu-N-C active sites. The catalyst delivers excellent performance over a wide pH range (1−13) and achieves a remarkable degradation rate of 97.7 % within 1 min under alkaline conditions (pH = 11). ESR and radical scavenging experiments confirm the generation of both radical ($\bullet O_2^-$) and non-radical ($^1O_2$) species during PMS activation. The Cu-N-C sites promote electron transfer and PMS activation. In addition, the catalyst exhibits exceptional stability and reusability. However, the current powder form may limit practical application due to challenges in catalyst separation and recovery during large-scale continuous treatment. Future work will focus on integrating this catalyst into membrane or fixed-bed systems to enable efficient recovery and long-term industrial use. Biological toxicity assessment confirms the high potential in large-scale environmental applications. The degradation mechanism is explored systematically. In summary, the results provide valuable insights into the design of stable, efficient, and recyclable biomass-derived carbon materials for PMS activation suitable for environmental remediation.

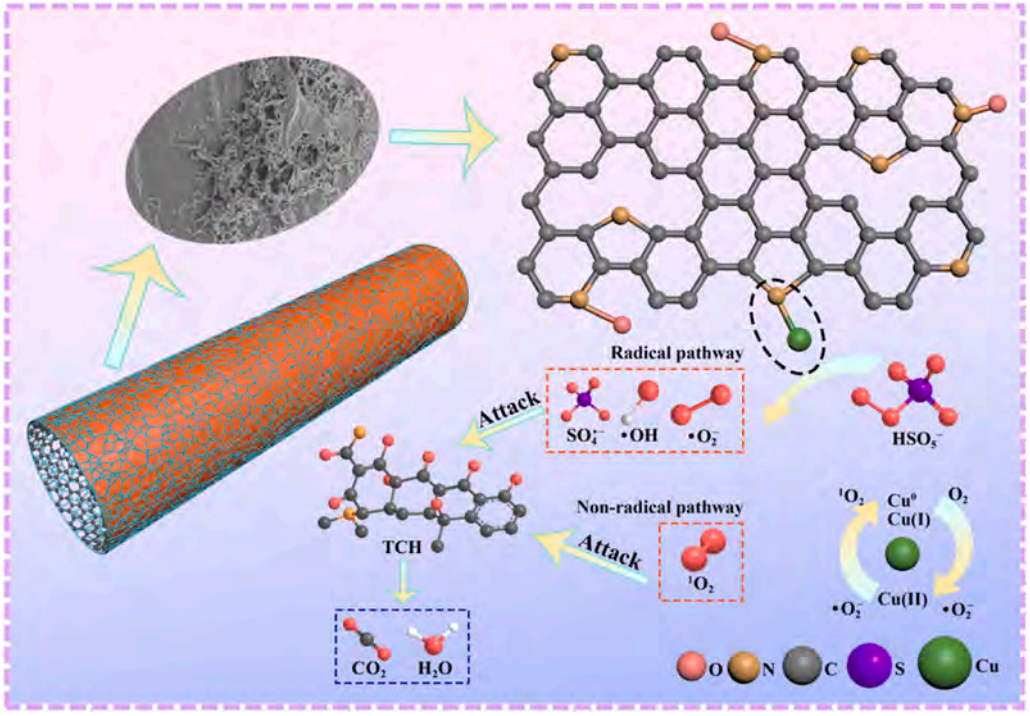

Fig. 11. Proposed mechanism of catalytic degradation by 0.6-Cu-N-KTC/PMS.

Declaration of Competing Interest

There are no conflicts of interest.

Acknowledgments

This study was financially supported by the National Natural Science Foundation of China (22108110, 22108106, 22308300), Jiangsu Engineering Laboratory of New Materials for Sewage Treatment and Recycling (SDGC2304). Natural Science Foundation of Jiangsu Province (BK20220598), City University of Hong Kong Donation Research Grants (DON-RMG No. 9229021 and 9220061), and Key Laboratory of Electrochemical Energy Storage and Energy Conversion of Hainan Province (No. KFKT2024005).

Appendix A. Supporting information

Supplementary data associated with this article can be found in the online version at doi:10.1016/j.jece.2025.119735.

Data availability

Data will be made available on request.

References

[1] A.B. Boxall, J.L. Wilkinson, A. Bouzas-Monroy, Medicating nature: are human-use pharmaceuticals poisoning the environment? One Earth 5 (2022) 1080–1084.
[2] L. Xiao, J. Liu, J. Ge, Dynamic game in agriculture and industry cross-sectoral water pollution governance in developing countries, Agric. Water Manag. 243 (2021) 106417.
[3] N. Ahmad, C.-F.J. Kuo, M. Mustaqeem, A. Sangili, C.-C. Huang, H.-T. Chang, Synthesis of novel Type-II $MnNb_2O_6$/g-C_3N_4 Mott-Schottky heterojunction photocatalyst: excellent photocatalytic performance and degradation mechanism of fluoroquinolone-based antibiotics, Chemosphere 321 (2023) 138027.
[4] Y. Shang, X. Xu, B. Gao, S. Wang, X. Duan, Single-atom catalysis in advanced oxidation processes for environmental remediation, Chem. Soc. Rev. 50 (2021) 5281–5322.
[5] D. Li, S. Zhang, S. Li, J. Tang, T. Hua, F. Li, Mechanism of the application of single-atom catalyst-activated PMS/PDS to the degradation of organic pollutants in water environment: a review, J. Clean. Prod. 397 (2023) 136468.
[6] X. He, X. Yang, C. Zhang, Y. Xiao, Y. Tang, Catalytic degradation of bisphenol a by heterogeneous bimetal composite carbon in the PMS and H_2O_2 systems: performance and mechanism, J. Clean. Prod. 414 (2023) 137571.
[7] G. Liu, Z. Liu, Y. Sun, M. Sun, J. Duan, Y. Tian, D. Du, M. Li, Cascade amplifying electrochemical bioanalysis for zearalenone detection in agricultural products: utilizing a Glucose–Fenton–HQ system on Bimetallic–ZIF@CNP nanocomposites, Foods 13 (2024) 3192.
[8] W. Qin, J. Peng, J. Yang, Y. Song, J. Ma, UV absorbance and electron donating capacity as surrogate parameters to indicate the abatement of micropollutants during the oxidation of Fe (II)/PMS and Mn (II)/NTA/PMS, Environ. Res. 232 (2023) 116253.
[9] Y. Fang, B. Qian, Y. Yang, Y. Song, Z. Yang, H. Li, Purification of high-arsenic groundwater by magnetic bimetallic MOFs coupled with PMS: balance of catalysis and adsorption and promotion mechanism of PMS, Chem. Eng. J. 432 (2022) 134417.
[10] Z. Li, X. Zhang, G. Li, F. Han, D. Hu, X. Huang, H. Yuan, Y. Tan, Hollow Co/CoO/Carbon nanofibers promoted PMS decomposition for the degradation of rhodamine b, J. Mater. Sci. Technol. 157 (2023) 120–129.
[11] H. Sun, B. Zhang, N. Wang, N. Zhang, Y. Ma, L. Zang, Z. Li, R. Xue, Refractory organics removal in PMS and H_2O_2/PMS oxidation system activated by biochar/nZVI/MoS_2 composite: synthesis, performance, mechanism and dosing methods, J. Environ. Chem. Eng. 11 (2023) 109134.
[12] F. Ghanbari, M. Moradi, Application of peroxymonosulfate and its activation methods for degradation of environmental organic pollutants, Chem. Eng. J. 310 (2017) 41–62.
[13] B. Wang, H. Chen, F. Huang, J. Liu, G. Liu, Y.-X. Weng, Y. She, X. Zhu, H. Li, J. Xia, Epitaxial $Bi_4O_5Br_2$ nanosheets on hollow carbon spheres for confined electron pump reactor and enhanced photocatalytic CO_2 hydrogenation reduction, Appl. Catal. B Environ. Energy 374 (2025) 125394.
[14] M. Kohantorabi, G. Moussavi, S. Giannakis, A review of the innovations in metal- and carbon-based catalysts explored for heterogeneous peroxymonosulfate (PMS) activation, with focus on radical vs. non-radical degradation pathways of organic contaminants, Chem. Eng. J. 411 (2021) 127957.
[15] G. Manickavasagam, C. He, K.-Y.A. Lin, M. Saaid, W.-D. Oh, Recent advances in catalyst design, performance, and challenges of metal-heteroatom-co-doped biochar as peroxymonosulfate activator for environmental remediation, Environ. Res. 252 (2024) 118919.
[16] B. Wang, J. Zhao, H. Chen, Y.-X. Weng, H. Tang, Z. Chen, W. Zhu, Y. She, J. Xia, H. Li, Unique Z-scheme carbonized polymer dots/$Bi_4O_5Br_2$ hybrids for efficiently boosting photocatalytic CO2 reduction, Appl. Catal. B Environ. Energy 293 (2021) 120182.
[17] J. Liu, H. Xu, Y. Xu, Y. Song, J. Lian, Y. Zhao, L. Wang, L. Huang, H. Ji, H. Li, Graphene quantum dots modified mesoporous graphite carbon nitride with significant enhancement of photocatalytic activity, Appl. Catal. B Environ. Energy 207 (2017) 429–437.
[18] Z. Tian, Q. Chen, S. Ren, H. Zhang, W. Tian, H. Sun, S. Wang, Effects of cobalt salts on biomass conversion to functional carbon-based catalysts for peroxymonosulfate activation, Chem. Eng. J. 469 (2023) 143856.

[19] J. Yang, L. Jing, X. Zhu, W. Zhang, J. Deng, Y. She, K. Nie, Y. Wei, H. Li, H. Xu, Modulating electronic structure of lattice O-modified orange polymeric carbon nitrogen to promote photocatalytic CO_2 conversion, Appl. Catal. B Environ. Energy 320 (2023) 122005.
[20] K. Zhu, C. Liu, W. Xia, Y. Wang, H. He, L. Lei, Y. Ai, W. Chen, X. Liu, Non-radical pathway dominated degradation of organic pollutants by nitrogen-doped microtube porous graphitic carbon derived from biomass for activating peroxymonosulfate: performance, mechanism and environmental application, J. Colloid Interface Sci. 625 (2022) 890–902.
[21] S. Shao, T. Sun, X. Li, Y. Wang, L. Ma, Z. Liu, S. Wu, Preparation of heavy bio-oil-based porous carbon by pyrolysis gas activation and its performance in the aldol condensation for aviation fuel as catalyst carrier, Ind. Crops Prod. 218 (2024) 118963.
[22] M. Zhu, L. Kong, M. Xie, W. Lu, H. Liu, N. Li, Z. Feng, J. Zhan, Carbon aerogel from forestry biomass as a peroxymonosulfate activator for organic contaminants degradation, J. Hazard. Mater. 413 (2021) 125438.
[23] C.-M. Hung, C.-W. Chen, C.-P. Huang, C.-D. Dong, Activation of peroxymonosulfate by nitrogen-doped carbocatalysts derived from brown algal (Sargassum duplicatum) for the degradation of polycyclic aromatic hydrocarbons in marine sediments, J. Environ. Chem. Eng. 9 (2021) 106420.
[24] S. Xin, S. Huo, C. Zhang, X. Ma, W. Liu, Y. Xin, M. Gao, Coupling nitrogen/oxygen self-doped biomass porous carbon cathode catalyst with $CuFeO_2$/biochar particle catalyst for the heterogeneous visible-light driven photo-electro-Fenton degradation of tetracycline, Appl. Catal. B Environ. Energy 305 (2022) 121024.
[25] W. Yang, C. Liu, B. Zhang, C. Wu, Y. Cao, W. Huang, W. Xu, Construction of a nitrogen-doped carbon quantum dot fluorescent molecularly imprinted sensor for ultra-sensitive detection of sulfadiazine in pork samples, Food Anal. Methods 17 (2024) 1689–1701.
[26] W. Ma, N. Wang, Y. Du, P. Xu, B. Sun, L. Zhang, K.-Y.A. Lin, Human-hair-derived N, S-doped porous carbon: an enrichment and degradation system for wastewater remediation in the presence of peroxymonosulfate, ACS Sustain. Chem. Eng. 7 (2018) 2718–2727.
[27] X. Liang, Y. Zhao, B. Liu, J. Li, L. Cui, C. Wang, Q. Yang, Phosphorus doped magnetic biochar activated PMS for effective degradation of pesticide in water: targeted regulation of interfacial charge transfer by phosphorus doping, Sep. Purif. Technol. 340 (2024) 126739.
[28] X. Gao, B. Wang, J. Liu, X. Zhu, X. Zhu, S. Zhu, C. Huang, Q. Ruan, D. Li, L. Liu, Structural design of hierarchical porous biomass carbon with a built-in electric field for efficient peroxymonosulfate activation, Chem. Eng. J. 499 (2024) 156075.
[29] H. Wang, W. Guo, B. Liu, Q. Wu, H. Luo, Q. Zhao, Q. Si, F. Sseguya, N. Ren, Edge-nitrogenated biochar for efficient peroxydisulfate activation: an electron transfer mechanism, Water Res. 160 (2019) 405–414.
[30] L. Xu, B. Fu, Y. Sun, P. Jin, X. Bai, X. Jin, X. Shi, Y. Wang, S. Nie, Degradation of organic pollutants by Fe/N co-doped biochar via peroxymonosulfate activation: synthesis, performance, mechanism and its potential for practical application, Chem. Eng. J. 400 (2020) 125870.
[31] S. Zhu, Q. Ruan, X. Zhu, D. Li, B. Wang, C. Huang, L. Liu, F. Xiong, J. Yi, Y. Song, Co single atom coupled oxygen vacancy on $W_{18}O_{49}$ nanowires surface to construct asymmetric active site enhanced peroxymonosulfate activation, J. Colloid Interface Sci. 664 (2024) 736–747.
[32] W. Chen, X. Li, X. Wei, G. Liao, J. Wang, L. Li, Activation of peroxymonosulfate for degrading ibuprofen via single atom cu anchored by carbon skeleton and chlorine atom: the radical and non-radical pathways, Sci. Total Environ. 858 (2023) 160097.
[33] W. Li, X. Hu, Q. Li, Y. Shi, X. Zhai, Y. Xu, Z. Li, X. Huang, X. Wang, J. Shi, Copper nanoclusters@nitrogen-doped carbon quantum dots-based ratiometric fluorescence probe for lead (II) ions detection in porphyra, Food Chem. 320 (2020) 126623.
[34] B. Wang, W. Zhang, G. Liu, H. Chen, Y.X. Weng, H. Li, P.K. Chu, J. Xia, Excited electron-rich $Bi^{(3-x)+}$ sites: a quantum well-like structure for highly promoted selective photocatalytic CO_2 reduction performance, Adv. Funct. Mater. 32 (2022) 2202885.
[35] G. Liu, L. Li, B. Wang, N. Shan, J. Dong, M. Ji, W. Zhu, P.K. Chu, J. Xia, H. Li, Construction of Bi nanoparticles loaded BiOCl nanosheets ohmic junction for photocatalytic CO_2 reduction, Acta Phys. Chim. Sin. 40 (2024) 2306041.
[36] H. Fan, C. Chen, J. Lu, C. Tan, P. Wang, J. Hu, X. Lu, X. Huang, A novel strategy for efficient utilization of carbon residue from biomass gasification loaded $NiCo_2O_4$ to construct composite catalysts for activation of peroxymonosulfate to effectively remove antibiotics, Sep. Purif. Technol. 335 (2024) 126196.
[37] F. Chen, X.-L. Wu, L. Yang, C. Chen, H. Lin, J. Chen, Efficient degradation and mineralization of antibiotics via heterogeneous activation of peroxymonosulfate by using graphene supported single-atom Cu catalyst, Chem. Eng. J. 394 (2020) 124904.
[38] Q. Wu, Y. Zhang, H. Meng, X. Wu, Y. Liu, L. Li, Cu/N co-doped biochar activating PMS for selective degrading paracetamol via a non-radical pathway dominated by singlet oxygen and electron transfer, Chemosphere 357 (2024) 141858.
[39] C. Ma, Y. Guo, D. Zhang, Y. Wang, N. Li, D. Ma, Q. Ji, Z. Xu, Metal-nitrogen-carbon catalysts for peroxymonosulfate activation to degrade aquatic organic contaminants: rational design, size-effect description, applications and mechanisms, Chem. Eng. J. 454 (2023) 140216.
[40] M. Ahmad, M. Yousaf, Waste to wonder: sustainable photocatalytic biochar from agro-plastic waste for advanced wastewater treatment, J. Environ. Chem. Eng. 13 (2025) 118374.
[41] D. Wang, P. Wang, B. Lu, K. Ye, K. Zhu, Q. Wang, J. Yan, G. Wang, D. Cao, Biomass-derived, nitrogen-rich carbon tubes as anodes for sodium-ion hybrid capacitors, ChemElectroChem 8 (2021) 4380–4388.
[42] Q. Zhou, J.-N. Kim, K.-W. Han, S.-W. Oh, S. Umrao, E.J. Chae, I.-K. Oh, Integrated dielectric-electrode layer for triboelectric nanogenerator based on Cu nanowire-mesh hybrid electrode, Nano Energy 59 (2019) 120–128.
[43] J. Kim, M. Kim, H. Jung, J. Park, Y. Lee, Ultrastable 2D material-wrapped copper nanowires for high-performance flexible and transparent energy devices, Nano Energy 106 (2023) 108067.
[44] P. Wu, S. Ma, S. Zhou, Y. Sun, L. Chen, J. Liu, W. Zhu, C. Xu, Fe_3N nanoparticles confined in h-BN for ultra-deep oxidative desulfurization using molecular oxygen, Chem. Eng. Sci. 305 (2025) 121136.
[45] N. Ahmad, C.-F.J. Kuo, M. Mustaqeem, M.K. Hussien, K.-H. Chen, Improved photocatalytic activity of novel $NiAl_2O_4$/g-C_3N_4 binary composite for photodegradation of 2, 4-dinitrophenol and CO_2 reduction via gas phase adsorption, Mater. Today Phys. 31 (2023) 100965.
[46] B. Wang, H. Chen, W. Zhang, H. Liu, Z. Zheng, F. Huang, J. Liu, G. Liu, X. Yan, Y. X. Weng, Semimetallic bismuthene with Edge-Rich dangling bonds: broad-spectrum-driven and edge-confined electron enhancement boosting CO_2 hydrogenation reduction, Adv. Mater. 36 (2024) 2312676.
[47] P. Wu, B. Wang, H. Li, S. Ma, L. Chen, J. Liu, Y. Chao, W. Zhu, C. Xu, Deep extractive denitrogenation with Cu-based ionic liquids and mechanistic insights, AIChE J. 71 (2025) e18739.
[48] Y. Li, Z. Liu, Y. Yang, H. Li, G. Qu, J. Zhao, P. Ning, K. Li, Typical MOFs-derived nanoporous carbon: insight into structures, properties and Pb (II) adsorption mechanism, Carbon 228 (2024) 119325.
[49] K.S. Sing, R.T. Williams, Physisorption hysteresis loops and the characterization of nanoporous materials, Adsorpt. Sci. Technol. 22 (2004) 773–782.
[50] G. Greczynski, L. Hultman, X-ray photoelectron spectroscopy: towards reliable binding energy referencing, Prog. Mater. Sci. 107 (2020) 100591.
[51] Z. Li, C. Guo, J. Lyu, Z. Hu, M. Ge, Tetracycline degradation by persulfate activated with magnetic Cu/$CuFe_2O_4$ composite: efficiency, stability, mechanism and degradation pathway, J. Hazard. Mater. 373 (2019) 85–96.
[52] A. Davó-Quiñonero, I. Such-Basanez, J. Juan-Juan, D. Lozano-Castello, P. Stelmachowski, G. Grzybek, A. Kotarba, A. Bueno-Lopez, New insights into the role of active copper species in CuO/Cryptomelane catalysts for the CO-PROX reaction, Appl. Catal. B Environ. 267 (2020) 118372.
[53] Q. Zhao, J. Sun, S. Li, C. Huang, W. Yao, W. Chen, T. Zeng, Q. Wu, Q. Xu, Single nickel atoms anchored on nitrogen-doped graphene as a highly active cocatalyst for photocatalytic H_2 evolution, ACS Catal. 8 (2018) 11863–11874.
[54] K.L. Oguzie, M. Qiao, E.E. Oguzie, The effect of humic acid on oxidative degradation of anthracene using cobalt ion-activated peroxymonosulfate, Inorg. Chem. Commun. 156 (2023) 111131.
[55] H.-J. Lee, H.-E. Kim, M.S. Kim, C.-F. de Lannoy, C. Lee, Inactivation of bacterial planktonic cells and biofilms by Cu (II)-activated peroxymonosulfate in the presence of chloride ion, Chem. Eng. J. 380 (2020) 122468.
[56] P. Neta, R.E. Huie, A.B. Ross, Rate constants for reactions of inorganic radicals in aqueous solution, J. Phys. Chem. Ref. Data 17 (1988) 1027–1284.
[57] Y. Liu, J. Gao, Y. Wang, W. Duan, J. Liu, Y. Zhang, H. Zhang, M. Zhao, The removal of antibiotic resistant bacteria and genes and inhibition of the horizontal gene transfer by contrastive research on sulfidated nanoscale zerovalent iron activating peroxymonosulfate or peroxydisulfate, J. Hazard. Mater. 423 (2022) 126866.

Supporting information

Synergistic PMS Activation by N-Bridged Spider-Web-Like Nanocopper Wires on Kapok-Derived Carbon for Efficient Removal of Organic Pollutants

Shenghui Wang[a], Yanhua Song[a*], Bin Wang[b,c], Xingwang Zhu[d], Xue Gao[b], Zhiyi Xu[b], Fujing Zhang[a], Jinyuan Liu[b,c*], Paul K. Chu[c*]

[a] *School of Environmental and Chemical Engineering, Jiangsu University of Science and Technology, Zhenjiang, Jiangsu 212003, P. R. China*

[b] *Institute for Energy Research, School of the Environment and Safety Engineering, Jiangsu University, Zhenjiang, Jiangsu 212013, P. R. China*

[c] *Department of Physics, Department of Materials Science and Engineering, and Department of Biomedical Engineering, City University of Hong Kong, Tat Chee Avenue, Kowloon, Hong Kong, China*

[d] *Institute of Technology for Carbon Neutralization, College of Environmental Science and Engineering, Yangzhou University, Yangzhou 225009, China*

***Corresponding authors**: songyh@just.edu.cn (Y.H. Song); jyliu@ujs.edu.cn (J.Y. Liu); paul.chu@cityu.edu.hk (P.K. Chu)*

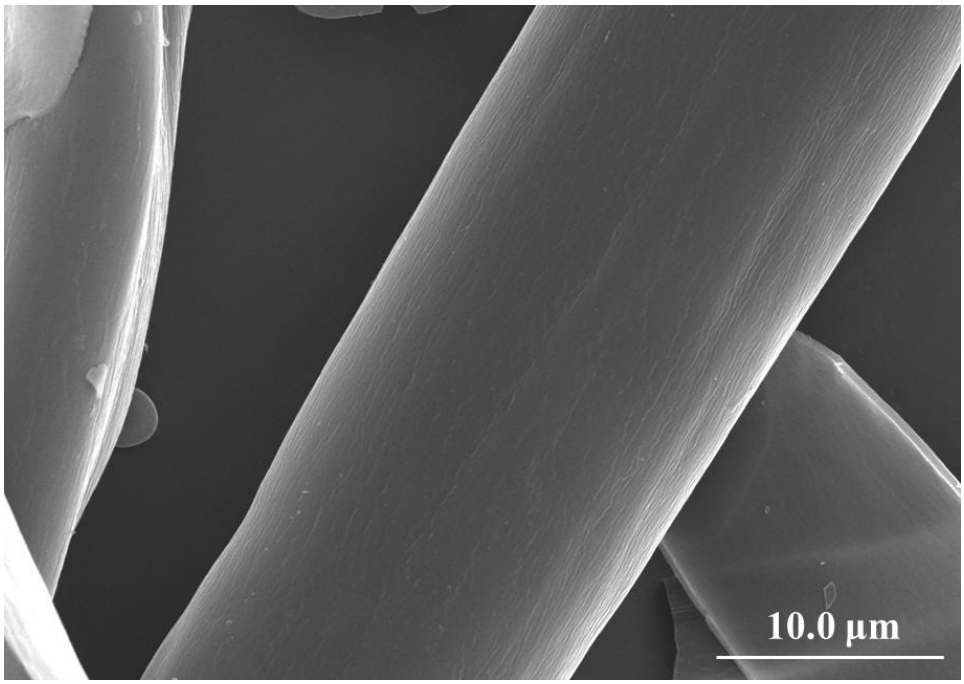

Figure S1. SEM image of KTC.

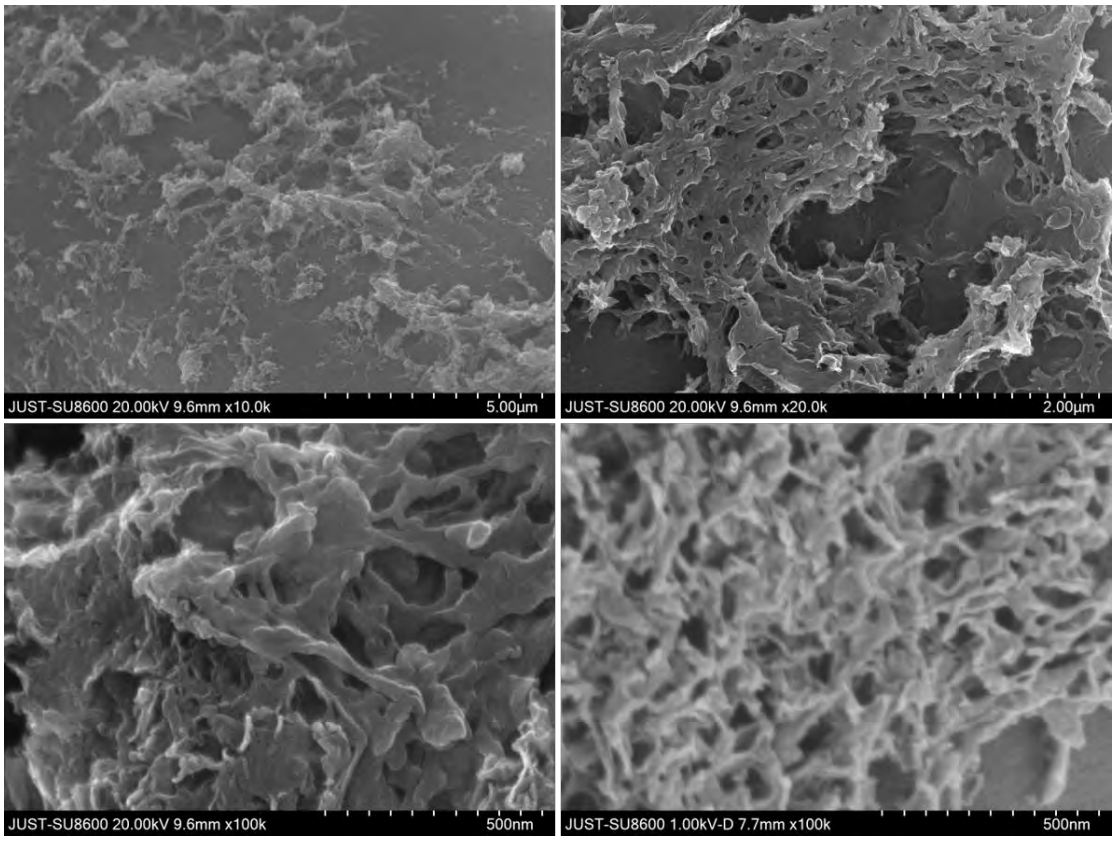

Figure S2. SEM images of 0.6-Cu-N-KTC.

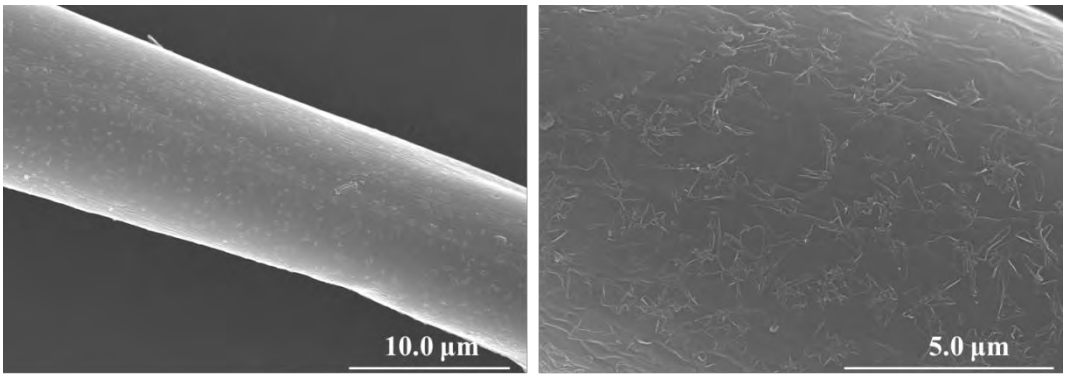

Figure S3. SEM images of 0.6-Cu-KTC.

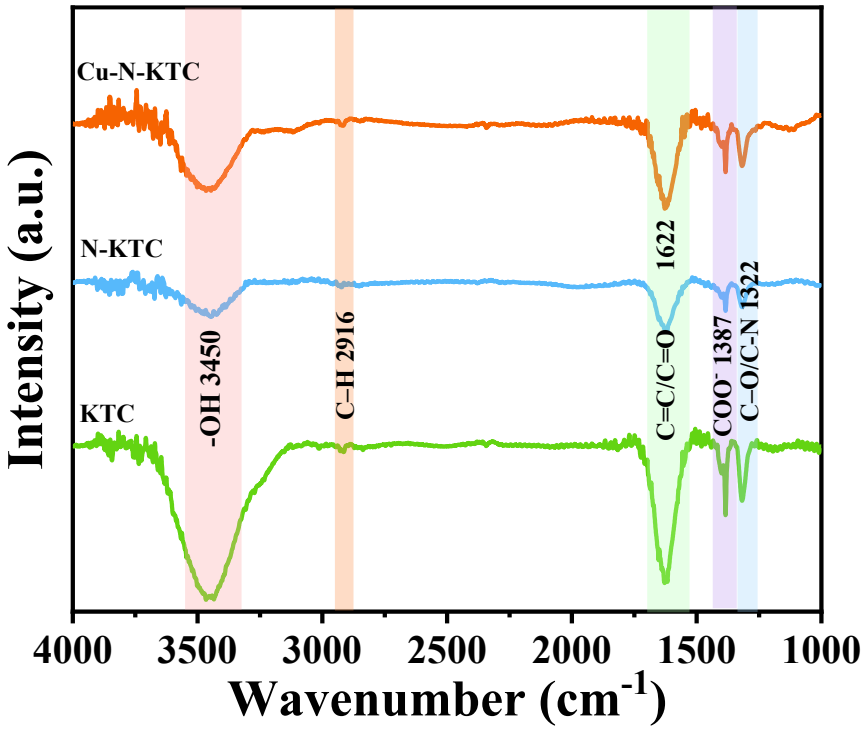

Figure S4. FTIR spectra of KTC, N-KTC, 0.6-Cu-N-KTC.

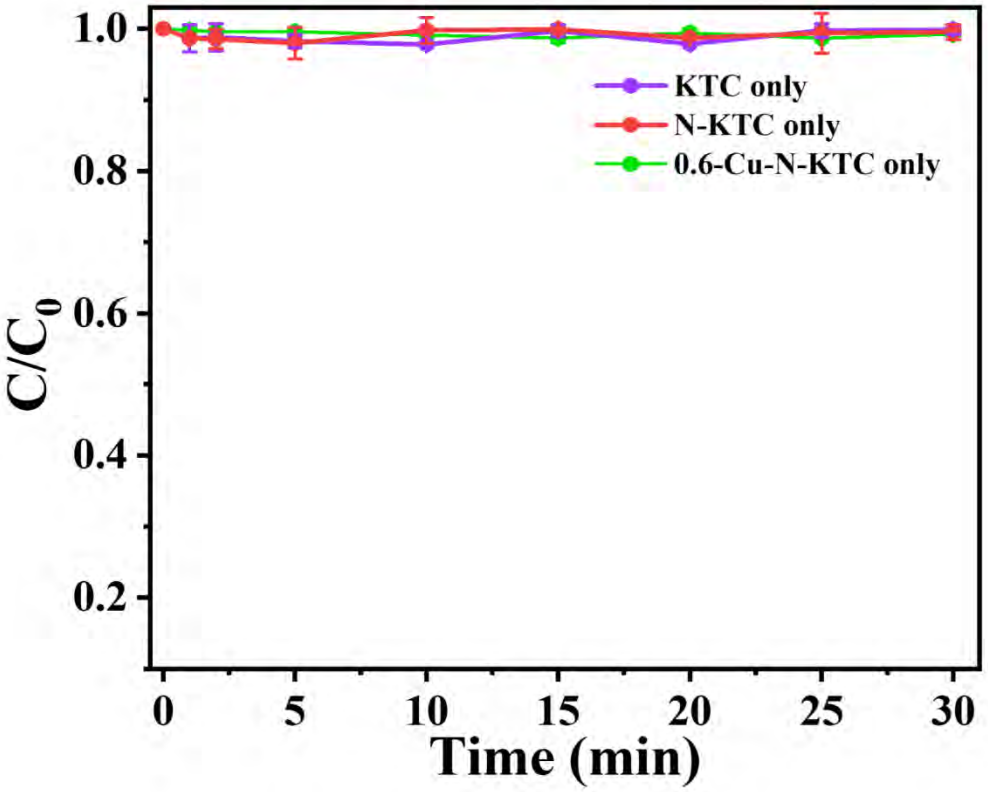

Figure S5. Degradation efficiency of TCH without PSM.

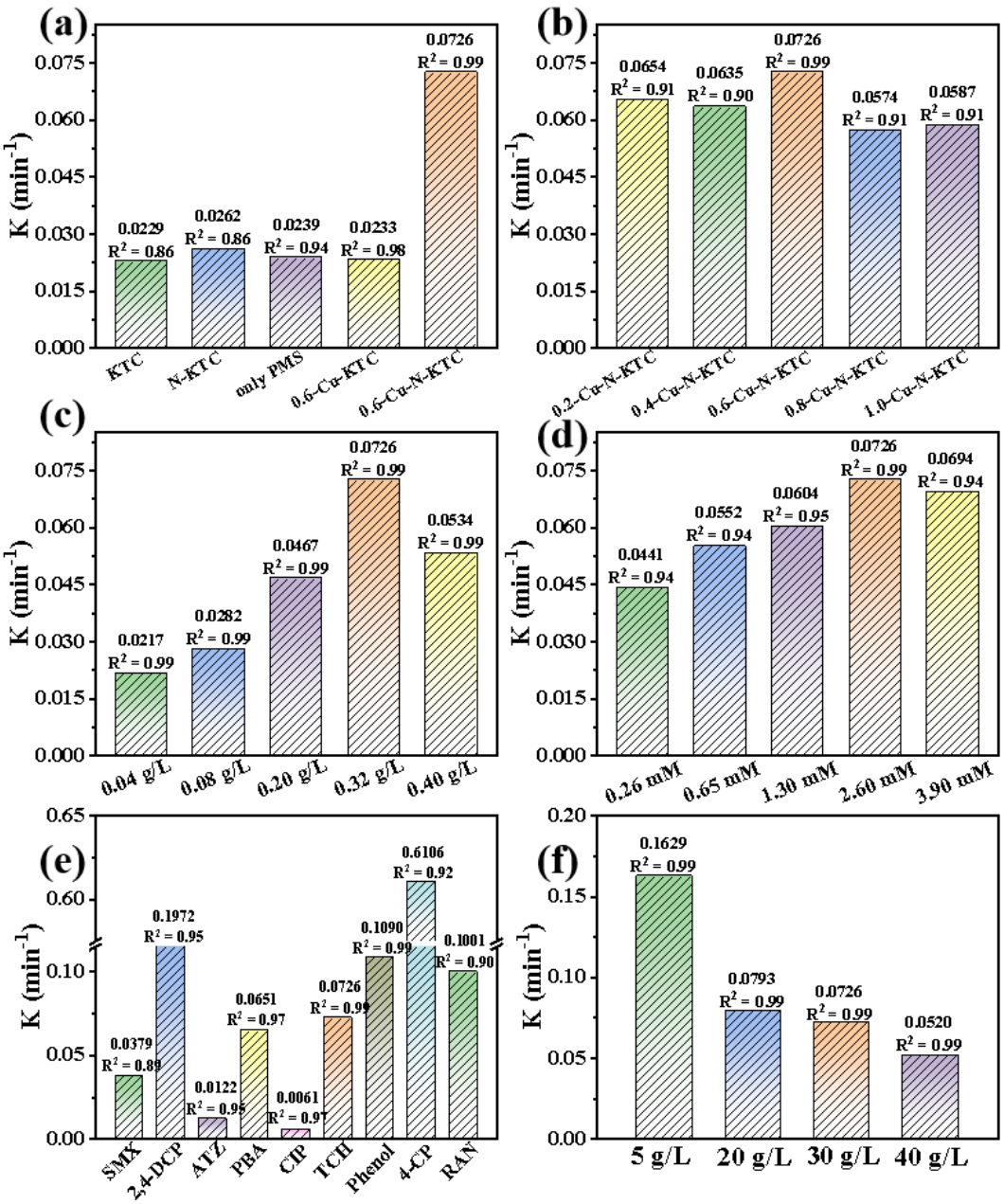

Figure S6. First-order degradation rate constants.

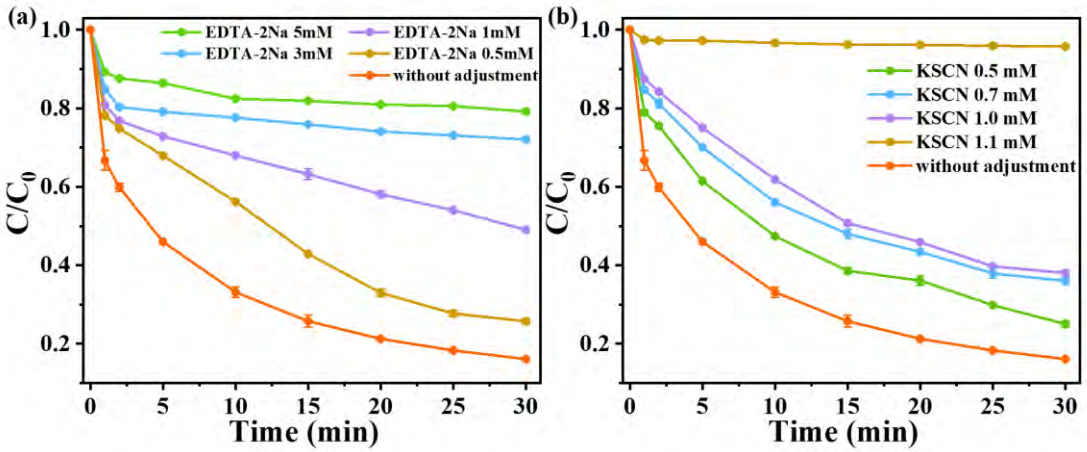

Figure S7. Effects of (a) EDTA-2Na and (b) KSCN concentrations as sacrificial agents on TCH degradation determined by two parallel experiments.

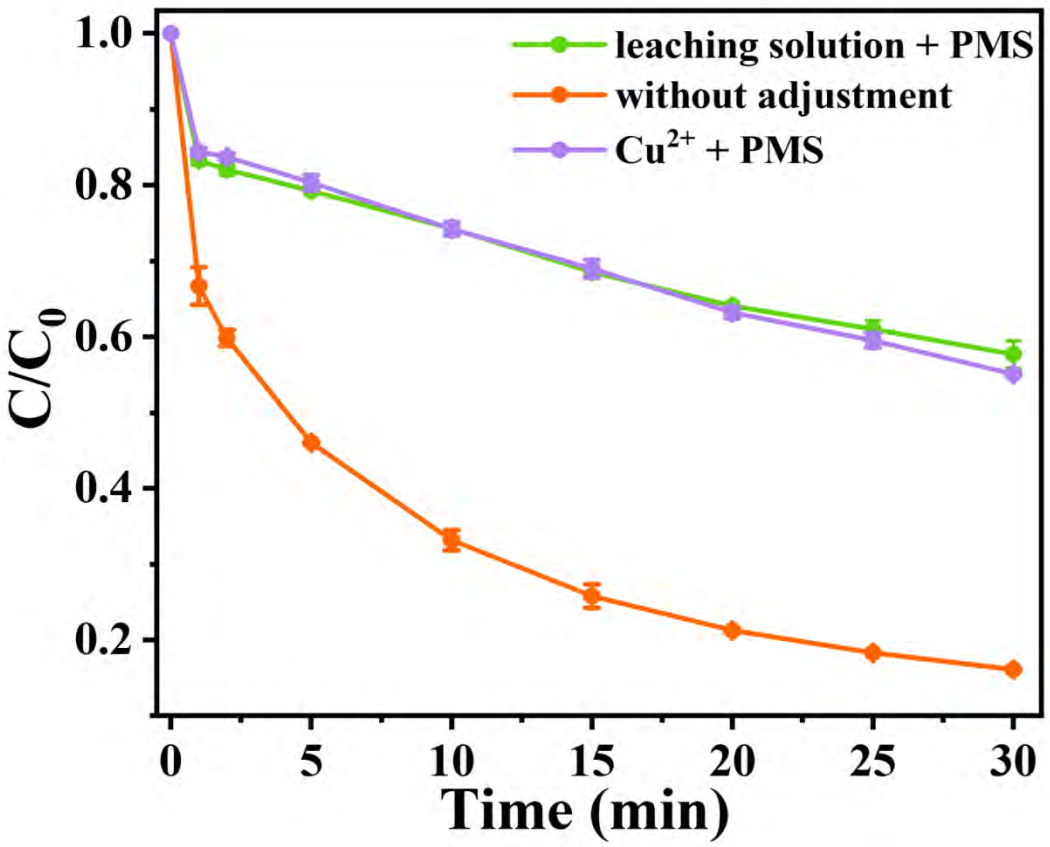

Figure S8. TCH removal efficiency of the homogeneous reactions with 0.4 mg/L Cu^{2+} and leaching solution determined by two parallel experiments.

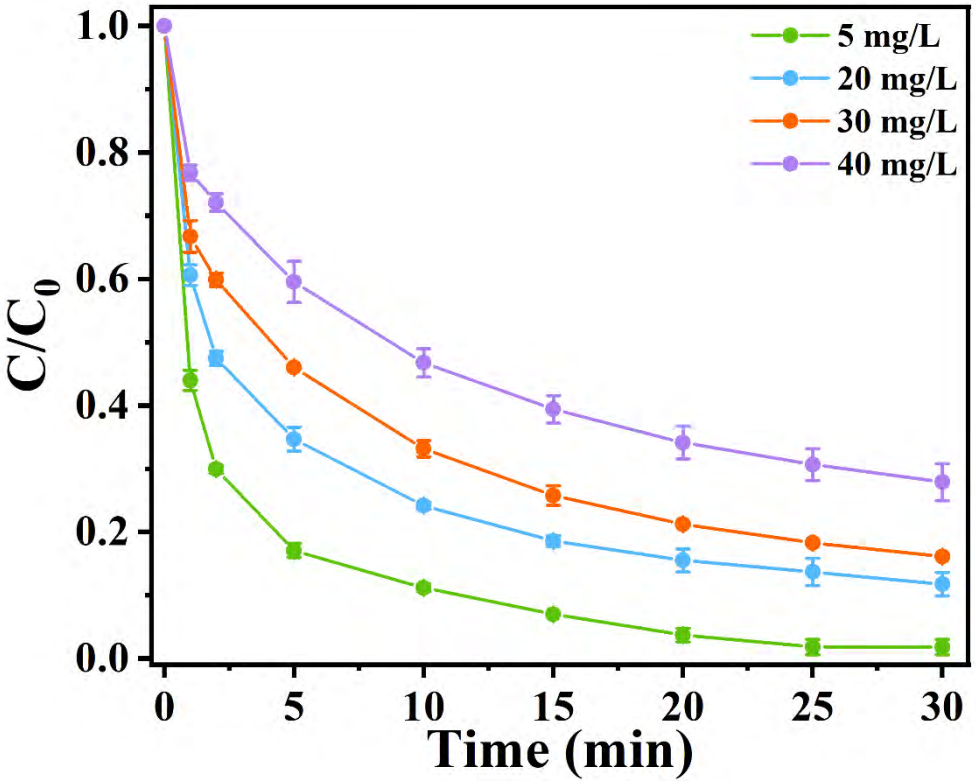

Figure S9. Effects of TCH concentrations on TCH degradation determined by two parallel experiments.

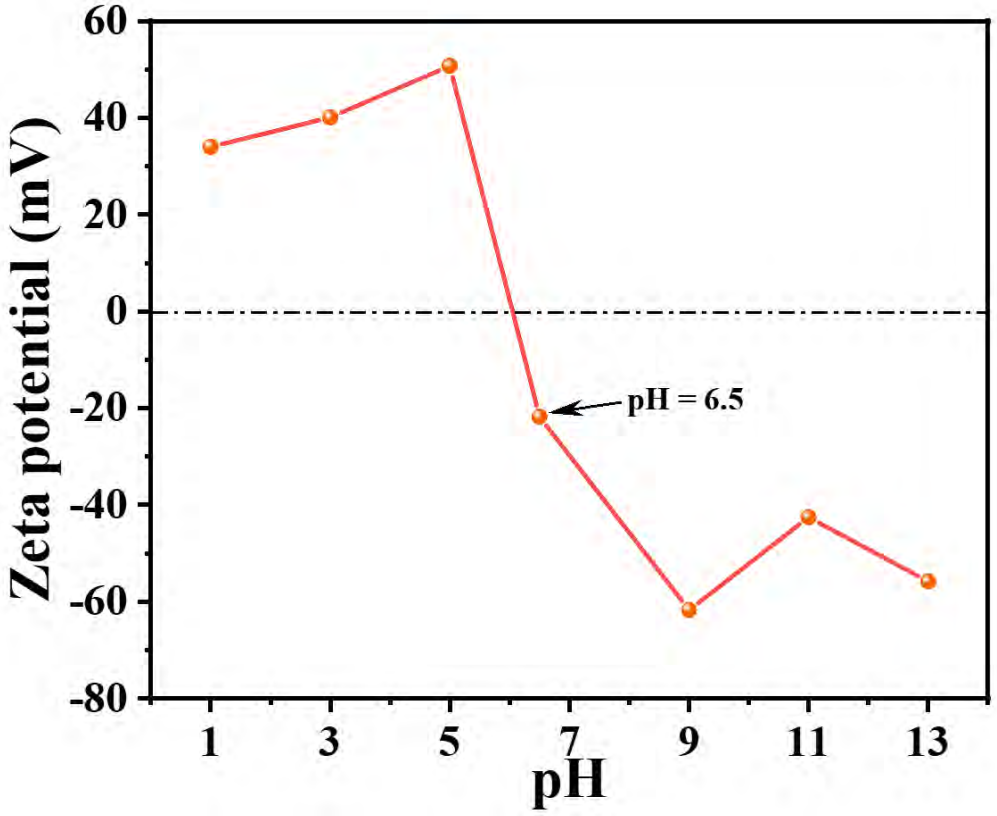

Figure S10. Zeta-potentials of 0.6-Cu-N-KTC dispersion solution at various pH values.

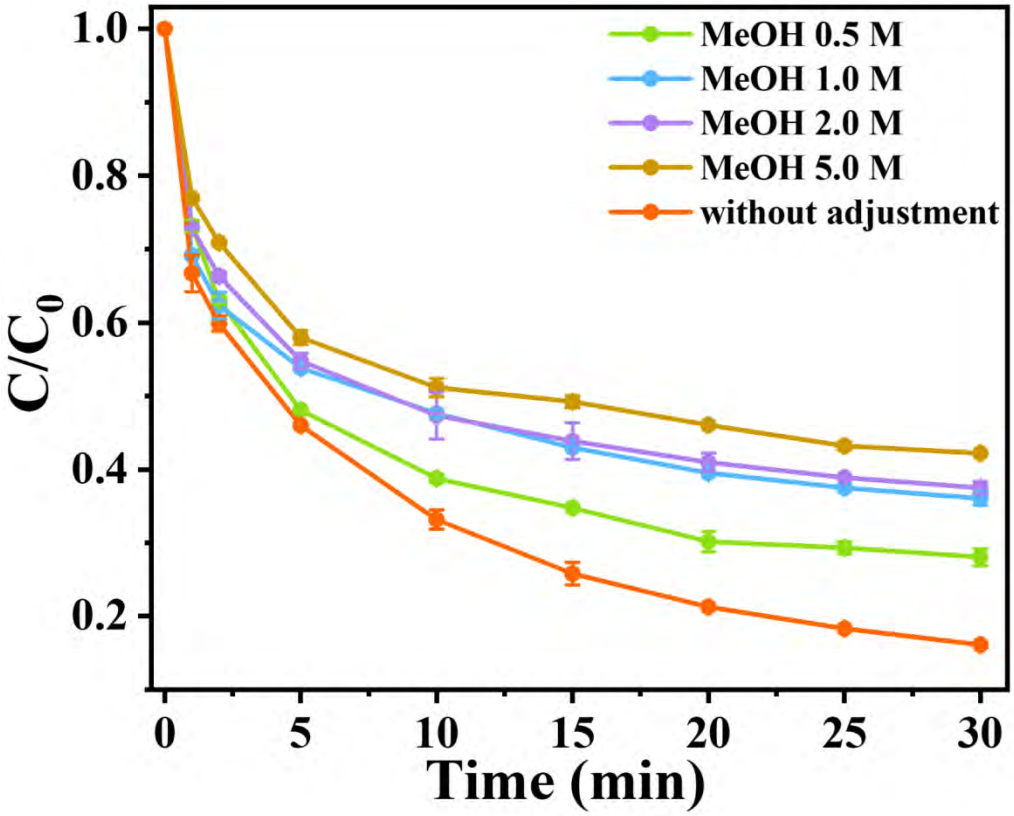

Figure S11. Effects of MeOH concentrations as sacrificial agents on TCH degradation determined by two parallel experiments.

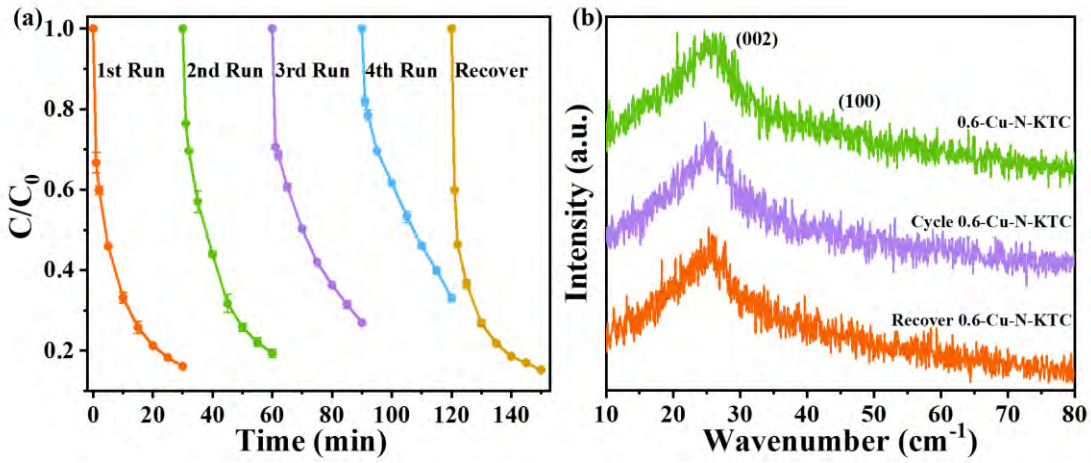

Figure S12. (a) Recycling characteristics of 0.6-Cu-N-KTC for TCH removal and (b) XRD patterns of pristine, cycled, and recovered 0.6-Cu-N-KTC determined by two parallel experiments.

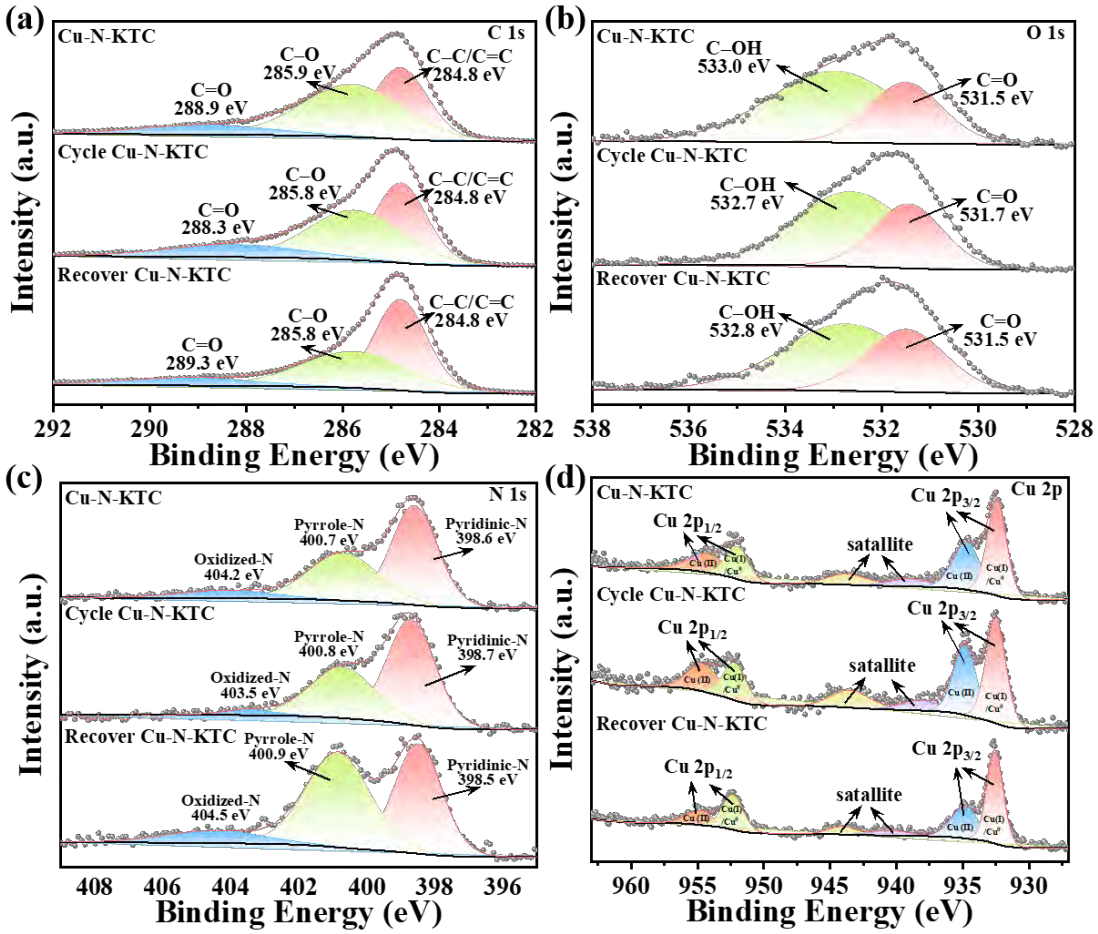

Figure S13. High-resolution XPS spectra: (a) C 1*s*, (b) O 1*s*, (c) N 1*s*, and (d) Cu 2p spectra of pristine, cycled, and recovered 0.6-Cu-N-KTC.

Table S1. Comparison of the kinetics of organic contaminant degradation with the use of PMS in recently reported PMS-based Fenton-like reactions.

Catalyst	Pollutant (mg/L)	PMS (mM)	Catalyst (g/L)	kobs (min^{-1})
This work	30	2.6	0.37	0.0726
Fe-N_4SAC [S1]	10	1	0.1	0.088
SA Cu/Graphene [S2]	10	1.3	0.1	0.087
Fe–Co–O–g-C_3N_4 [S3]	10.1	0.8	0.2	0.085
$LaMnO_3$-Cu-6 [S4]	5	1.3	0.2	0.058
BNSBC [S5]	10	2	0.3	0.0408
DMDB-800 [S6]	15	2.5	1	0.0245
NRGO [S7]	10.1	0.8	0.5	0.0101

References

[S1] Lin, Y., Wang, Y., Weng, Z., Zhou, Y., Liu, S., Ou, X., ... & Yang, Z. (2024). Coordination engineering of heterogeneous high-valent Fe (IV)-oxo for safe removal of pollutants via powerful Fenton-like reactions. *Nature Communications*, *15*(1), 10032.

[S2] Chen, F., Wu, X. L., Yang, L., Chen, C., Lin, H., & Chen, J. (2020). Efficient degradation and mineralization of antibiotics via heterogeneous activation of peroxymonosulfate by using graphene supported single-atom Cu catalyst. Chemical Engineering Journal, 394, 124904.

[S3] Wang, S., Liu, Y., & Wang, J. (2020). Peroxymonosulfate activation by Fe–Co–O-codoped graphite carbon nitride for degradation of sulfamethoxazole. Environmental Science & Technology, 54(16), 10361-10369.

[S4] Gao, P., Tian, X., Fu, W., Wang, Y., Nie, Y., Yang, C., & Deng, Y. (2021). Copper in LaMnO3 to promote peroxymonosulfate activation by regulating the reactive oxygen

species in sulfamethoxazole degradation. Journal of Hazardous Materials, 411, 125163.

[S5] Wang, H., Zhang, Q., Ji, H., Zhang, Y., Fu, B., Wu, Y., & Ding, Y. (2024). Boron and nitrogen hydrothermal co-doped sludge biochar towards efficiently activate peroxymonosulfate for sulfamethoxazole degradation. Journal of Cleaner Production, 466, 142843.

[S6] Wang, Y., Song, Y., Li, N., Liu, W., Yan, B., Yu, Y., ... & Wang, S. (2022). Tunable active sites on biogas digestate derived biochar for sulfanilamide degradation by peroxymonosulfate activation. Journal of Hazardous Materials, 421, 126794.

[S7] Wang, S., Xu, L., & Wang, J. (2019). Nitrogen-doped graphene as peroxymonosulfate activator and electron transfer mediator for the enhanced degradation of sulfamethoxazole. Chemical Engineering Journal, 375, 122041.